International Journal of Biological Macromolecules 375 (2026) 153423

Contents lists available at ScienceDirect

International Journal of Biological Macromolecules

journal homepage: www.elsevier.com/locate/ijbiomac

Modulation of early aggregation events by flexible peptidomimetics inhibits gelsolin amyloid formation

Michela Bollati [a,1], Kaliroi Peqini [b,1], Carmina Natale [c], Federica Malinverno [a,d], Chiara Leonardi [a,c], Beatrice Bonaldi [b], Loic Girois [a], Katiuscia Pagano [d], Laura Ragona [d], Alessandro Corbelli [c], Fabio Fiordaliso [c], Andrea Grazzi [e], Xinyue Gao [e], Stefano Pieraccini [e], Sara Pellegrino [b,1], Luisa Diomede [c,1], Matteo de Rosa [a,*,1]

[a] Institute of Biophysics, National Research Council (IBF-CNR), via A. Corti 12, 20133, Milano, Italy
[b] Department of Pharmaceutical Science, "A. Marchesini" General and Organic Chemistry Section, University of Milano, Via Venezian 21, 20133, Milano, Italy
[c] Department of Molecular Biochemistry and Pharmacology, Istituto di Ricerche Farmacologiche Mario Negri IRCCS, Via Mario Negri 2, 20156, Milano, Italy
[d] CNR-SCITEC, Institute of Science and Chemical Technologies "Giulio Natta" (SCITEC-CNR), Via Corti 12, 20133, Milano, Italy
[e] Department of Chemistry, University of Milan, Via Golgi 19, 20133 Milano, Italy

ARTICLE INFO

Keywords:
Gelsolin Amyloidosis
Gelsolin
Aggregation
Peptidomimetics
C. elegans

ABSTRACT

Gelsolin amyloidosis (Agel) is a hereditary systemic disorder caused by point mutations in the gelsolin (GSN) gene that promote aberrant proteolytic processing and deposition of amyloidogenic fragments. The most prevalent variant, D187N, destabilizes the G2 domain of the protein and exposes a cleavage site, ultimately generating fragments containing the GSN amyloidogenic core. Targeting this sequence represents a promising therapeutic strategy.

Here, we report a comprehensive structural and mechanistic characterization of LB6, a rationally designed peptidomimetic inhibitor of gelsolin aggregation, together with selected analogues. Biophysical, computational, and structure-activity relationship analyses reveal that LB6 populates a dynamic ensemble of conformations whose flexibility is critical for activity. LB6 and its reverse-sequence analogue MC35 effectively inhibit fibril formation and promote remodelling of pre-formed aggregates of the pathogenic G2 domain, carrying D187N mutation ($G2_{D187N}$). Mechanistic studies indicate that these compounds interfere with early events of $G2_{D187N}$ aggregation and counteract the toxicity of aggregated $G2_{D187N}$ *in vivo* in *C. elegans*. Collectively, our results identify conformational adaptability as an important determinant of inhibitory potency and establish LB6 as a promising lead scaffold for the development of therapeutic agents targeting AGel.

1. Introduction

Gelsolin amyloidosis (AGel) refers to a hereditary amyloidosis with worldwide distribution caused by mutations in the gelsolin *GSN* gene [1–13]. Patients experience a slow, progressive neurological deterioration characterized by corneal lattice dystrophy, cutis laxa, and sensory polyneuropathy, ultimately affecting nearly all organs [14,15]. This decline results from the accumulation of amyloidogenic gelsolin (GSN) fragments in multiple tissues. GSN is a calcium-dependent regulator of actin filament dynamics, composed of six homologous domains, G1 to G6 [16–20]. AGel is caused by single-point substitutions in two main regions of the protein: the first close to the calcium-binding site in the second domain (G2-linked) and the second spot at the interface between G4 and G5 domains [1,11,21,22]. The first identified and most common mutation, D187N/Y [8], triggers the deposition of amyloid fibrils in the walls of blood vessels and perineural sheaths, affecting nearly all organs [14]. The aggregation mechanism is initiated by the destabilization of the G2 domain, triggered by the substitution of residue D187, which is part of the G2 calcium-binding site, with either N or Y. This mutation impairs Ca^{2+}-binding and consequently disrupts key interactions with partner residues within the G2 core. As a result, a furin cleavage site that would normally remain buried within the stable domain core is exposed and available for cleavage during secretion in the trans-Golgi environment [23–26]. The cleavage in the second domain releases a 68 kDa

* Corresponding author.
E-mail address: matteo.derosa@cnr.it (M. de Rosa).
[1] These authors contributed equally.

https://doi.org/10.1016/j.ijbiomac.2026.153423
Received 20 May 2026; Received in revised form 30 June 2026; Accepted 7 July 2026
Available online 9 July 2026

fragment that is further processed in the extracellular matrix by metalloproteases, producing 8- and 5-kDa amyloidogenic fragments, A_{173}-M_{243} and A_{173}-R_{225}, respectively. Both fragments contain the amyloidogenic core 182-SFNNGDCFILD-192 ($GAC_{182–192}$).

Full-length GSN, in the wild-type (WT) form and in the G2 variants, shows a weak propensity to aggregate under physiological conditions. In contrast, the isolated G2 domain, which is around thirty residues longer than the 8-kDa fragment, shows a strong tendency to aggregate [27]. G2 fibrillogenesis follows a typical sigmoidal kinetic curve that can be fitted with quantitative models to elucidate the underlying aggregation mechanism. Like other known amyloidogenic proteins, the β-sheet-rich structures formed by G2 form toxic oligomeric intermediates that act as nuclei for protofibril and fibril formation [28–31]. The characterization of this process is essential for understanding disease pathogenesis and developing anti-aggregation therapies.

To date, no pharmacological treatments are available for AGel. Patients rely on invasive and short-term interventions, such as the surgical excision of amyloid deposits. However, multiple strategies are currently being explored to improve patient outcomes and quality of life. The various approaches mainly target the stabilization of the G2 domain rescuing mutant GSN misfolding or inhibiting the aggregation process by using nanobodies and Fab antibodies [24,32–37]. Small molecules, such as non-selective polyphenols, phospholipids, peptidomimetics, and other repurposed drugs, are under investigation to counteract fibril aggregation and toxicity [27,38–42]. In this context, we have recently designed a set of peptidomimetics to inhibit aggregation of the GSN_{D187N} variant [27], designed based on the three-dimensional native structure of $G2_{D187N}$. They contain a portion of $GAC_{182–192}$ and a flanking β-strand 194-GNNIHQWCGSN-204 ($FS1_{194–204}$), linked by an unnatural piperidine-pyrrolidine amino acid [43]. Among the synthesized compounds, LB6 was the most promising in terms of solubility and anti-aggregating activity, showing a strong effect on both $GAC_{182–192}$ itself and the entire $G2_{D187N}$ domain.

Here we report the structural characterization of LB6 peptide and its activity on $G2_{D187N}$ domain aggregation. Both experimental and computational studies demonstrated that LB6 exists as an ensemble of rapidly interconverting conformations, and this conformational flexibility may be essential for its biological activity. Structure-activity relationship studies indicated that the specific amino acid sequence, and the presence of all structural components are also determinants for LB6's activities. Overall, LB6 and its reversed-sequence analogue, MC35, are able to interfere with early aggregation events and to affect the morphology of pre-formed fibrils. The nematode *C. elegans* was then employed to investigate whether the properties of the two peptides translate into a protective effect *in vivo*. This nematode is a well-established biosensor for the toxicity of misfolded proteins, including GSN [27]. LB6 and MC35 reduced the toxicity associated with pre-formed $G2_{D187N}$ fibrils and their remodelling. These findings indicate that LB6 could serve as a scaffold for developing new therapeutic agents targeting AGel.

2. Results

2.1. The lead molecule - LB6 - populates a dynamic ensemble of conformations

The conformational behaviour of the LB6 peptidomimetic was investigated through a combination of solution-state NMR spectroscopy and all-atom molecular dynamics (AA-MD) simulations.

LB6 NMR spectra were first acquired in the absence of any reducing agent, to assess the potential formation of an intra-peptide disulphide bridge between the two Cysteines located in the two peptide arms. The absence of short-range inter-strand NOEs in NOESY/ROESY spectra excluded the presence of an intramolecular Cys188-Cys201 disulfide bridge and the spectra recorded under oxidizing conditions were perfectly superimposable to those recorded in the presence of dithiothreitol (DTT) over 24 h, which is the timescale of the $G2_{D187N}$ aggregation experiments (see Supplementary Fig. S1). Only traces of sulfenic acid were obtained under harsh oxidizing conditions (see Supplementary Table S1), further supporting that the formation of a disulfide is unfavoured.

Residue level NMR investigation highlighted the presence of two distinct patterns of resonances for many residues located in both peptide arms, including I190, L191, H198, W200, C201, and S203, as illustrated in Fig. 1A, C. These duplicated signals indicate the presence of two conformational states in slow exchange on the millisecond timescale, most likely corresponding to alternate orientations of the piperidine linker. Complete chemical-shift assignments for residues G186–D187–C188–F189–I190–L191 and H198–Q199–W200–C201–G202–S203–N204 were obtained for both states (Supplementary Fig. S2 and Table S2). Secondary structure analysis from Hα and Cα chemical shifts (Fig. 1B, D) revealed predominantly random-coil behaviour, with only two transiently structured segments: a D187–I190 turn supported by an D187Hβ–I190γCH2 NOE, and a C201–S203 turn indicated by positive ΔδCα at G202–S203. The translational diffusion coefficient, measured form DOSY experiment, further confirms the intrinsically disordered, low-compactness nature of LB6 (Supplementary Fig. S3).

A complementary computational exploration of the conformations accessible to LB6 in aqueous solution, performed with all-atom molecular dynamics (AA-MD), supports the disordered structural landscape highlighted by NMR experiments. In particular, five independent replicas of well-tempered metadynamics (WT-metaD) [44] of 1 μs each were collected using the peptide's radius of gyration and a putative hydrogen bond network derived from a hypothetical β-hairpin configuration [44–46] as Collective Variables (CVs). The resulting free energy surfaces (FESs) have been averaged, allowing to recover the conformational landscape reported in Fig. 1E-F. The global minimum corresponds to conformations lacking β-hairpin-like hydrogen bonds. The radius of gyration can vary from 0.6 nm (compact conformation I) to 1.1 nm (open conformation II). A secondary minimum is found with just one internal hydrogen bond (conformation III). Interestingly, the FES surface recovered with the enhanced sampling approach (*i.e.*, WT-metaD) is coherent with the conformational clusters obtained from an equilibrium simulation of 500 ns, as reported in Supplementary Fig. S4.

Consistent with the transient ordering at the level of D187–I190 and C201–S203 regions, revealed by NMR, secondary structure analysis of AA-MD data with DSSP algorithm [47], suggested that those regions populate locally ordered conformations which are relatively conserved across LB6 conformations belonging to the two main basins (Supplementary Result 1 and Fig. S5). Overall, the experimental and MD data converge to show that LB6 behaves as a highly flexible, dynamic peptidomimetic with only local, transient structural elements, an intrinsic property that may contribute to its ability to interact with misfolded $G2_{D187N}$ intermediates.

2.2. Nucleation drives $G2_{D187N}$ aggregation as revealed by concentration and seeding effects

Before gaining insight into the mechanisms of action of LB6, as a promising inhibitor of GSN aggregation, we focused on the isolated G2 domain [24,48], carrying the pathogenic D187N mutation ($G2_{D187N}$). $G2_{D187N}$ also better recapitulates the fragments observed in AGel patients than the previously used GAC. To this end, aggregation of 5–25 μM $G2_{D187N}$ was monitored at 37 °C, pH 5.0, and under shaking conditions using ThT as an amyloid reporter dye. $G2_{D187N}$ aggregation followed a typical sigmoidal behaviour (Fig. 2A), with a relatively long lag phase. To better quantify the aggregation, the data were fit with the logistic function which describes general sigmoidal kinetics. From this equation, we extrapolated the amplitude of aggregation (A), which reflects the amount of β-sheet–rich amyloid fibrils, the length of the lag phase (t_{lag}), and τ, the midpoint of the growth phase (*i.e.*, how fast the combination of elongation and secondary nucleation occurs). A linear dependence on the natural logarithm (ln) of the $G2_{D187N}$ concentration was observed for

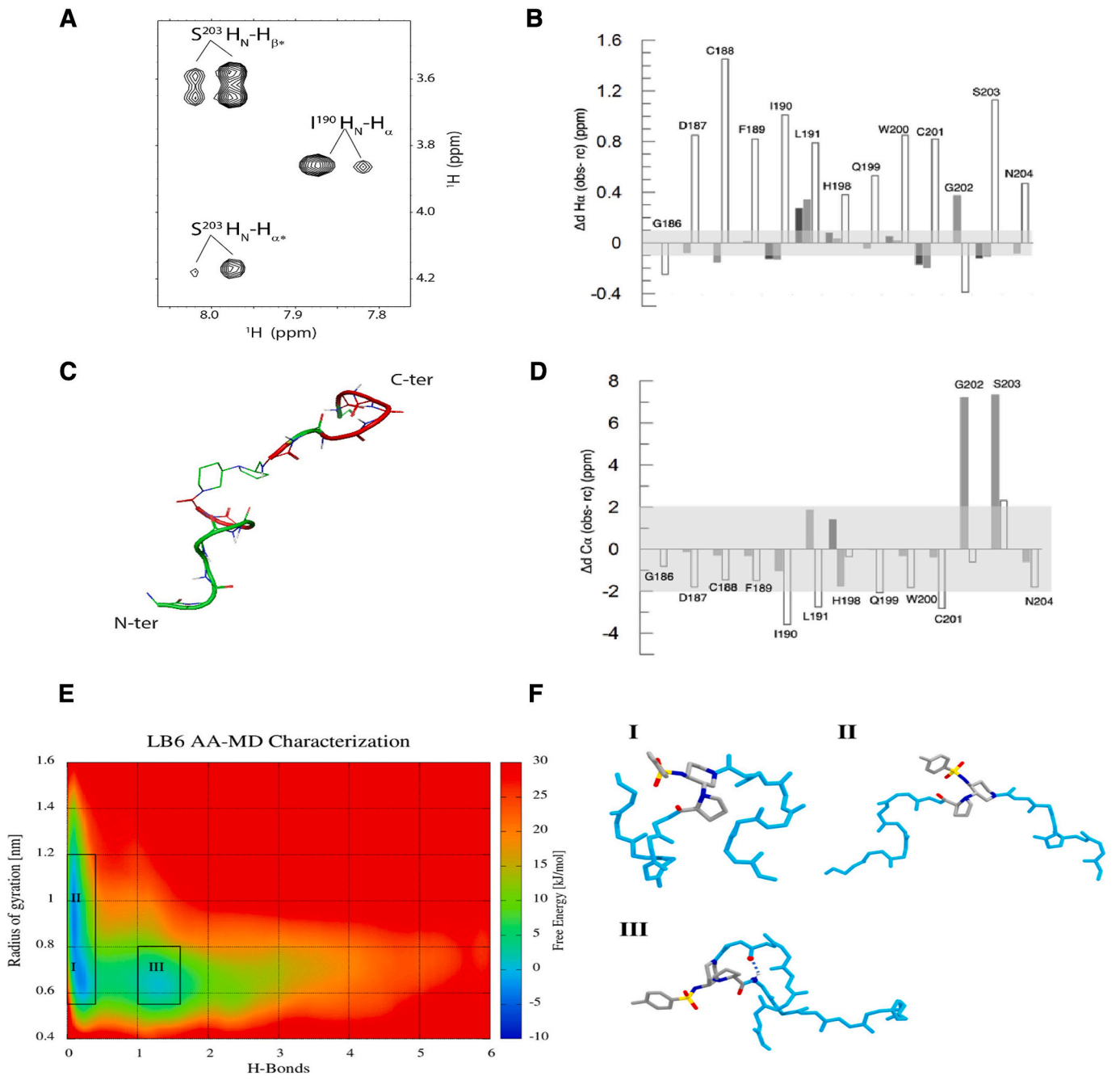

Fig. 1. NMR and AA-MD conformational analysis of LB6. A) Selected spectral region of LB6 $^{1}H—^{1}H$ TOCSY, the two patterns of signals are shown for specific residues. B) Residues showing two distinct conformations are shown in red on the peptide sequence. LB6 Secondary structure propensity: per residue Hα (C) and Cα (D) chemical shift analysis is reported. The differences between the chemical shift values determined experimentally for LB6 and the random coil are plotted as light grey bars. Dark bars are reported when two separated Hα/Cα are observed for a single residue. Empty bars show the secondary chemical shift values measured for G2 gelsolin domain (BMRB 4794). The shaded rectangles in C and D highlight significant variations. E) Average Free Energy Surface of LB6 in aqueous environment computed with WT-metaD. Black rectangles indicate CV-boundaries of the conformational basins. F) Representative poses of LB6 extracted from the highlighted regions in the FES. Conformations with no interchain hydrogen bond are represented by I (compact state) and II (open state). A secondary basin is represented by III, with one internal interchain hydrogen bond. For clarity, backbone atoms of the peptide chains have been coloured in light blue, while the synthetic linker moiety is represented in grey.

all parameters (Fig. 2B/C, Table 1), though to varying degrees. These results indicate that increasing monomer $G2_{D187N}$ concentration significantly accelerates nuclei formation (*t_lag* slope = −1.4 h ± 0.1), while having only a modest effect on fibril growth, (τ slope = −0.4 h ± 0.1), ultimately producing a larger amount of amyloids (Amplitude slope 1998 ± 218).

The D187N mutation increases the domain's conformational flexibility, yet $G2_{D187N}$ is a metastable, structured module that requires partial unfolding to expose aggregation-prone regions. The rate of this misfolding event may contribute to the onset of aggregation. To gain insights into the early events of aggregation, static ThT kinetic measurements of 15 μM $G2_{D187N}$ were performed in the presence of 0%, 10% (1.5 μM) and 40% (6 μM) sonicated preformed fibrils (Fig. 2D). As expected, the introduction of preformed fibrils mainly accelerated the onset of fibril growth. The reductions in the lag phase of ~35% and ~ 50% observed with the addition of 10% and 40% seeds, respectively,

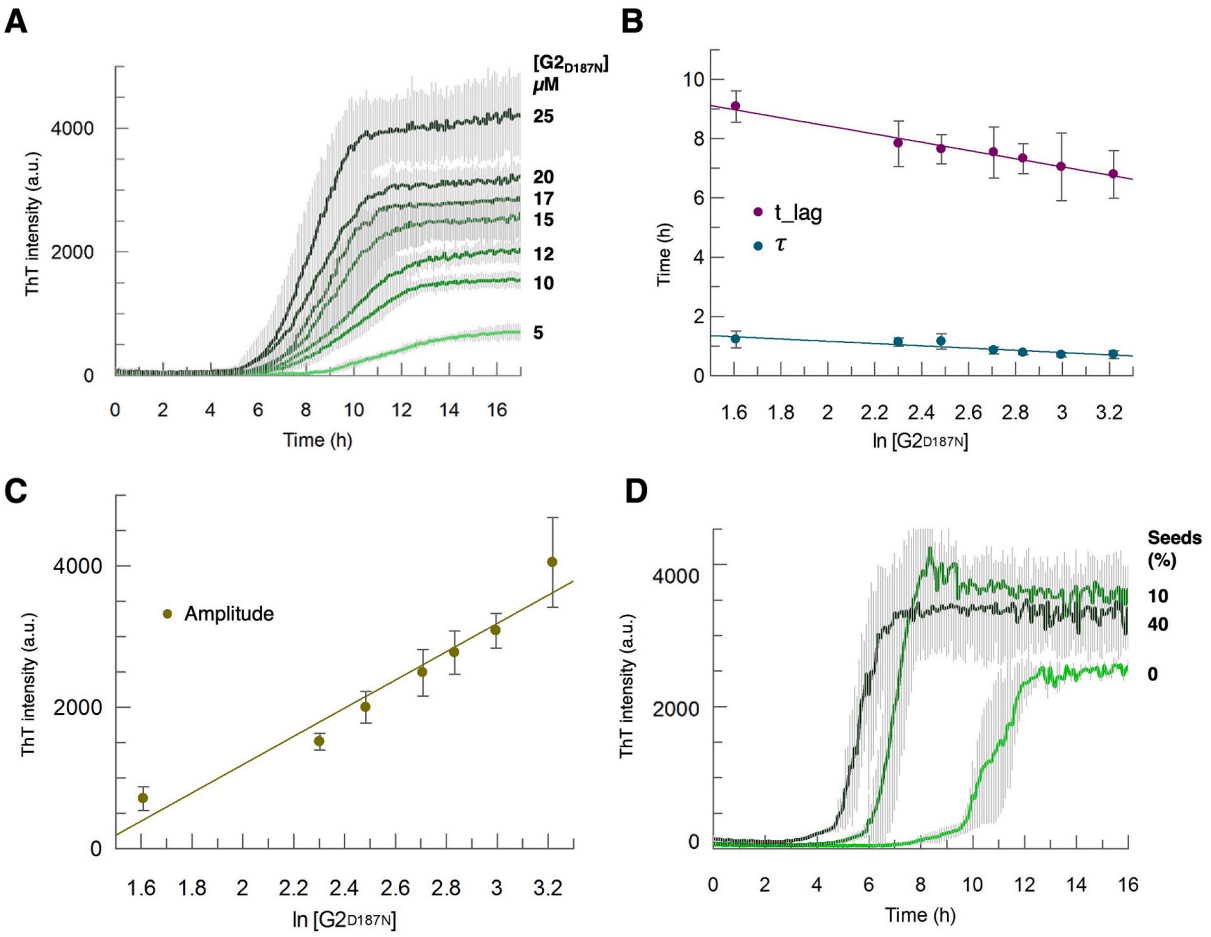

Fig. 2. Kinetics of $G2_{D187N}$ aggregation in the absence and presence of pre-formed fibrils. A) Aggregation kinetics of 5–25 μM $G2_{D187N}$ at 37 °C, pH 5.0, and under shaking conditions were followed by monitoring the ThT fluorescence intensity. Data are the mean ± SEM of $n \geq 3$ technical replicates and are representative of at least 3 independent experiments. B) Values of t_lag, τ, and C) Amplitude, resulting from the fitting with the logistic function, are interpolated by linear regression. Data are the mean ± SD ($n = 5$). D) Aggregation kinetics of 15 μM $G2_{D187N}$ at 37 °C, pH 5.0, performed without shaking, in the absence (0%) and in the presence of 10% and 40% of sonicated preformed fibrils (seeds).

Table 1
Kinetic parameters of $G2_{D187N}$ aggregation in the absence and presence of pre-formed fibrils. Values of t_lag (h), τ (h), and Amplitude (a.u.) calculated by fitting with a logistic equation the ThT values from aggregation kinetics of 5–25 μM $G2_{D187N}$ at 37 °C, pH 5.0, monitored under shaking conditions. Values of t_lag (h), τ (h), and Amplitude (a.u.) were also calculated from aggregation kinetics of 15 μM $G2_{D187N}$ at 37 °C, pH 5.0, monitored without shaking, in the absence (0%) and in the presence of 10% and 40% of sonicated preformed fibrils (seeds). Data are means ± SD from the fitting (n ≥ 3).

$G2_{D187N}$ (μM)	Shaking	Seeds (%)	*t_lag* (h)	*τ* (h)	Amplitude (a.u.)
5	✓	0	9.1 ± 0.5	1.2 ± 0.3	705.6 ± 168.5
10	✓	0	7.8 ± 0.8	1.1 ± 0.1	1512.1 ± 120.2
12	✓	0	7.6 ± 0.5	1.2 ± 0.3	1997.7 ± 224.9
15	✓	0	7.5 ± 0.9	0.9 ± 0.1	2487.2 ± 328.1
17	✓	0	7.3 ± 0.5	0.8 ± 0.1	2771.3 ± 305.6
20	✓	0	7.0 ± 1.1	0.7 ± 0.1	3082.4 ± 247.1
25	✓	0	6.8 ± 0.8	0.7 ± 0.1	4047.3 ± 635.7
15	–	0	9.3 ± 0.9	0.3 ± 0.02	2452.0 ± 84.3
15	–	10	6.0 ± 0.5	0.2 ± 0.02	3534.6 ± 361.2
15	–	40	4.6 ± 0.3	0.3 ± 0.05	3218.0 ± 574.5

t_lag correspond to the time of growth onset; τ evaluate the rate of fibril growth; Amplitude (a.u.) is calculated by the difference between the fluorescence intensity of the plateau and the baseline.

indicated that *t_lag* is likely influenced by the rate of primary nucleation rather than misfolding of $G2_{D187N}$ (Table 1). Yet, the persistence of a measurable lag phase even at 40% seeding (strong seeding) suggests that additional kinetic processes, such as elongation or secondary nucleation, also influence the aggregation kinetics [49]. These kinetic parameters constitute the basis for the subsequent studies on the effect of LB6 on $G2_{D187N}$ aggregation, described in the following section.

2.3. LB6 slows down aggregation by inhibiting early aggregation events

The antiaggregating potential of LB6 on $G2_{D187N}$ was investigated using different experimental approaches. First, ThT aggregation kinetics of 25 μM $G2_{D187N}$ were monitored at 37 °C, pH 5, and shaking conditions, in the absence and presence of increasing LB6 concentration (0.1:1, 1:1, 10:1 LB6-to-$G2_{D187N}$ molar ratio). As shown in Fig. 3A, LB6 significantly alters the aggregation process in a concentration-dependent manner. The effect was already appreciable at a sub-stoichiometric inhibitor concentration, and aggregation was almost abolished at a 10:1 molar ratio. Visual inspection of the curve highlights a delay in the lag phase, but to better understand which process LB6 may affect, we analysed the curves using the logistic function. Quantitative analysis focused on the *t_lag* and *τ* (Fig. 3B and Supplementary Table S3). Amplitude (*A*) is generally considered not to be such a robust parameter. Fibril polymorphism and ligands may alter interactions with ThT and its signal, and an LB6 analogue later characterized serves as a notable example.

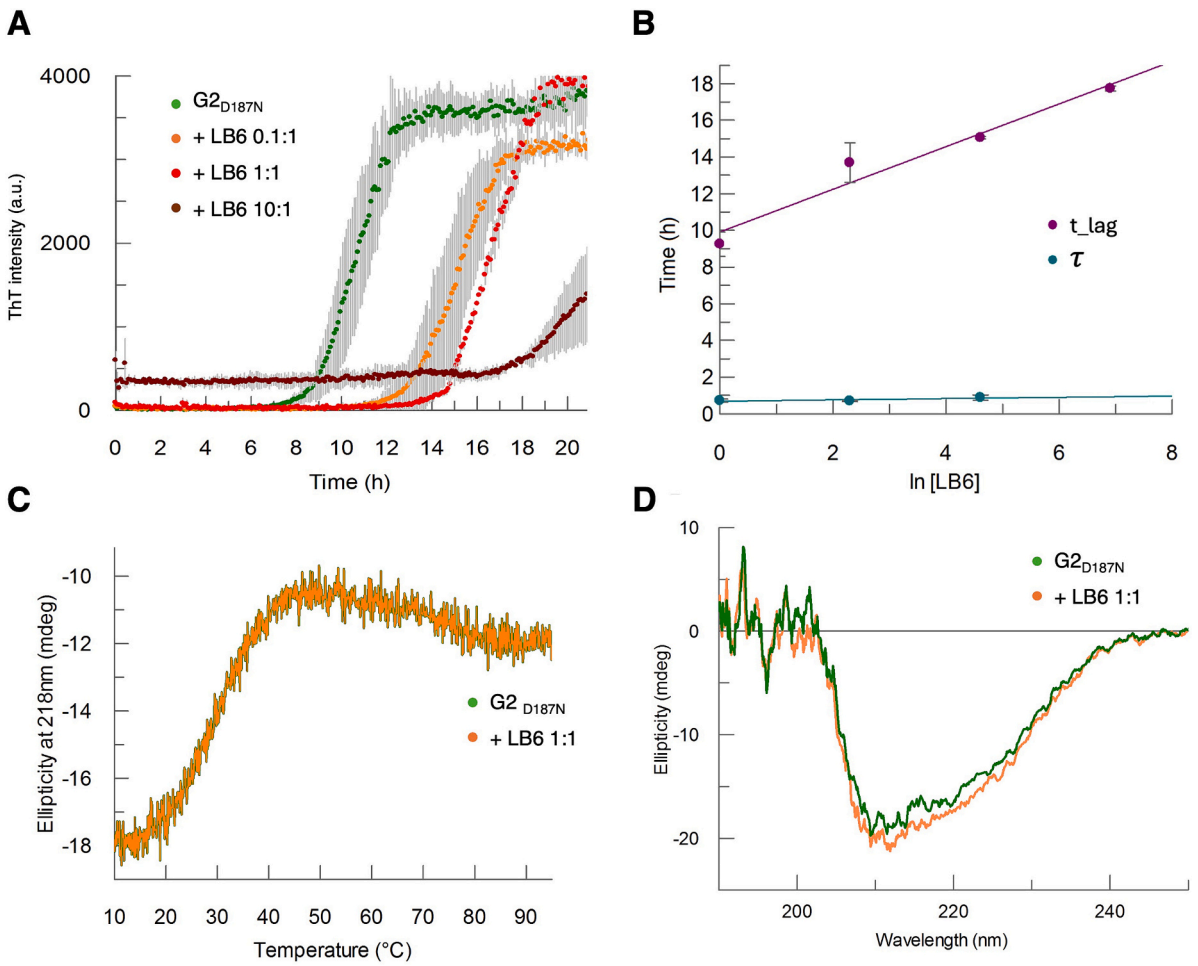

Fig. 3. Effect of LB6 on the aggregation, thermal stability, and secondary structure of $G2_{D187N}$. A) ThT aggregation curves of 25 μM $G2_{D187N}$, monitored at 37 °C and pH 5, in the absence and presence of different LB6 concentrations (0.1:1, 1:1, 10:1 LB6-to-$G2_{D187N}$ molar ratio). Data are the mean ± SEM of n ≥ 3 technical replicates from at least 3 independent experiments. B) Values of the t_lag and τ resulting from the fitting with the logistic function and interpolated by linear regression. Data are the mean ± SD (n = 5). C) Thermal denaturation of 15 μM $G2_{D187N}$, at pH 5, in the absence and presence of 15 μM LB6 (1:1 molar ratio), analysed by CD spectroscopy. D) Representative CD spectra, recorded at 10 °C, of 15 μM $G2_{D187N}$, at pH 5, in the absence and presence of 15 μM LB6 (1:1 molar ratio).

Both *t_lag* and *τ* showed a nearly linear dependence on the ln of LB6 concentration (Fig. 3B). However, the t_lag slope, equal to 1.2 h ± 0.2, was much higher compared to the slope of *τ* (0.03 h ± 0.02), and the increase of the parameter at the lowest concentration of inhibitor tested equal to +48% and 0%, respectively. These data suggest that LB6 had only a minor impact on elongation and/or secondary nucleation. Contrarily, there was a significant delay in the onset of fibril growth with a strong concentration-dependence. We showed that lag phase correlates with primary nucleation or other early aggregation events, but a similar delay could also result from stabilization of the native state, a mechanism of GSN aggregation inhibition we already described for the nanobody Nb11 [24].

To exclude a chaperone-like activity of LB6, we analysed its impact on the secondary structure and thermal stability of $G2_{D187N}$ at pH 5. The structural stability of 15 μM $G2_{D187N}$ in the absence and presence of LB6 (1:1 molar ratio) was studied by monitoring Far-UV CD signals at 218 nm as a function of temperature. The analysis of the curves using the software BestSel (https://bestsel.elte.hu/index.php) showed that the apparent melting temperature of $G2_{D187N}$ was 31.7 ± 0.9 °C (compared to 46.5 °C previously measured at pH 7.4 [23,24,48]), which remained unchanged in the presence of 15 μM LB6. Indeed, the curves for $G2_{D187N}$ alone and in the presence of LB6 fully overlapped (Fig. 3C), indicating that the peptidomimetic did not affect the protein's thermal stability. Likewise, the CD spectra showed no significant differences between $G2_{D187N}$ with and without LB6, both of which displayed an intense minimum centred around 210 nm (Fig. 3D), indicating no detectable LB6-induced alterations in the secondary structure of $G2_{D187N}$. These observations excluded any stabilizing or destabilizing effect of LB6 on $G2_{D187N}$.

2.4. Both structural and sequence determinants contribute to LB6 inhibitory activity

To further dissect the contribution of the LB6 structural determinants to its activity, we synthesized its isolated components, *i.e.* the piperidine-pyrrolidine scaffold, the amyloidogenic sequence $GAC_{184–191}$, the flanking $FS1_{194–204}$ sequence. Furthermore, we designed two other analogues: MC35, containing the two peptide arms in inverted position, and MC45, containing the alternative flanking sequence ($FS2_{160–166}$) flanking GAC in the native structure of G2 (Fig. 4A-B).

The piperidine-pyrrolidine scaffold was synthesized through a multicomponent reaction as in [50], while the flanking sequences FS1, FS2, and the peptidomimetics MC35 and MC45 were synthesized using solid-phase peptide synthesis (SPPS) [27]. To investigate the conformational propensities of all compounds, their CD spectra were recorded at a concentration of 100 μM in water and at pH 5 (Fig. 4C and Supporting Fig. S6). Owing to its poor water solubility, GAC was not analysed. Spectra of LB6 in water and in buffer showed the absence of a

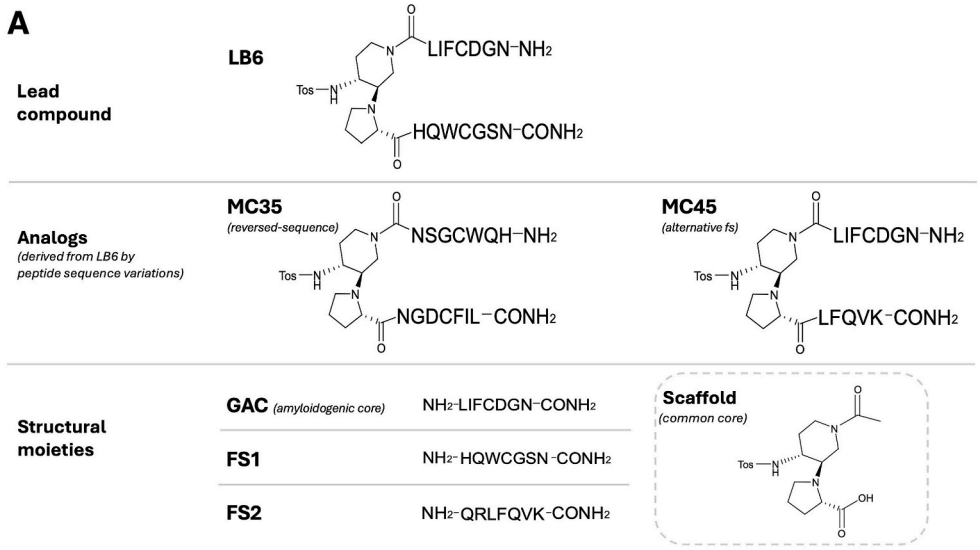

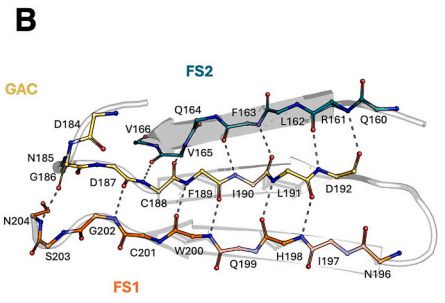

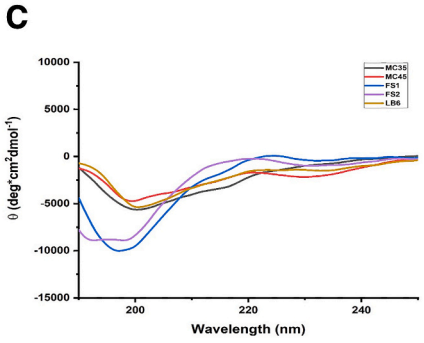

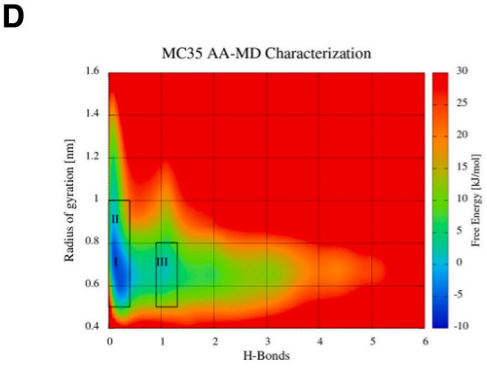

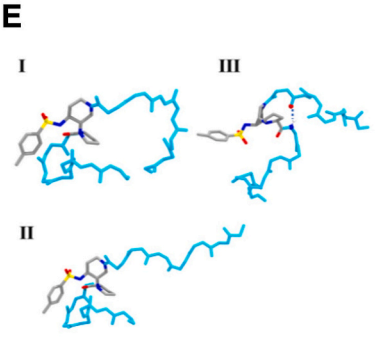

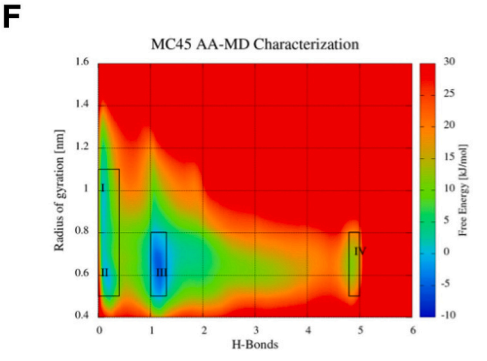

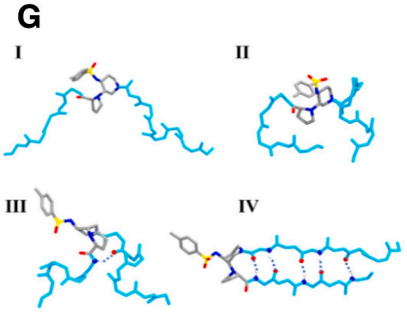

(caption on next page)

Fig. 4. Design and characterization of the peptidomimetics. A) Schematic structure of LB6, the analogues MC35 and MC45, the peptidic moieties, and the Scaffold [50]. B) The design of LB6 and its analogues was inspired by the conformation and localization of the gelsolin amyloidogenic core (GAC) in the native structure of the protein (pdb id 6QW3), [74]. A significant stretch of $GAC_{182–192}$ adopts a β-strand conformation and interacts with two flanking strands, $FS1_{194–204}$ (purple) and $FS2_{160–166}$ (blue). C) Representative CD spectra recorded for LB6, MC35, MC45, and the flanking regions FS1 and FS2 suspended in water at 100 μM. AA-MD characterization of D) MC35 and F) MC45 computed with WT-metaD. Black rectangles indicate CV-boundaries of the conformational basins. Representative poses of E) MC35 and G) MC45 extracted from the highlighted regions in the FES.

positive band at 190 nm and a negative band at 200 nm, indicating a lack of preferred conformation. On the other hand, a negative Cotton effect at 230 nm, and a shoulder at 215 nm, both typical of a β-structure, were also observed. Dichroweb analysis (Table 2) [51] confirmed the conformational freedom of LB6 described by NMR and MD, with a 53% of random population. The two flanking sequences, FS1 and FS2, were mostly unstructured, as evidenced by the minima below 200 nm. The two peptidomimetics, MC35 and MC45, on the other hand, showed a trend similar to LB6. Of relevance, MC45 showed a more intense negative peak at 230 nm, probably due to π-π interactions of the Phe rings present in the two peptide arms, suggesting the presence of a β-hairpin structure. This observation was confirmed by the Dichroweb conformational analysis reported in Table 2. MC45, indeed, showed a similar β-turn content together with a higher β-sheet percentage compared to the analogs (Table 2), diagnostic of a β-hairpin structure contribution.

Computational exploration of the conformational landscape for MC35 and MC45 was performed using the same simulation protocol as for LB6. The average FES obtained from five independent replicas of WT-metaD is reported in Fig. 4D for MC35. The behaviour of MC35 is comparable to LB6, with a high preference for conformations with no internal hydrogen bonds between the two strands of the putative β-hairpin (Fig. 4E). A secondary minimum was found for conformations that transiently form one hydrogen bond. Results for MC45 are reported in Fig. 4F, G. Interestingly, while the large basin describing unstructured conformations remains relevant, MC45 shows a higher degree of internal structuring. A well-defined minimum is found for structures with one internal interchain hydrogen bond. In addition, the β-hairpin-like conformation (conformation IV in Fig. 4G) was visited in three out of five WT-metaD simulations, resulting in a secondary but significant minimum in the final averaged FES. A comparison of the FES landscape predicted with WT-metaD with conformational clusters obtained from equilibrium AA-MD simulations is reported in Supplementary Fig. S4. For MC35, the two methodologies yield converged results. In contrast, for MC45, the poses observed over 500 ns of unbiased AA-MD populate only one of the possible basins (*e.g.*, the internally uncoordinated one), highlighting the importance of enhanced-sampling simulations to efficiently obtain a more comprehensive description of the conformational landscape.

The effects of the peptidomimetics and the single moieties on the aggregation kinetics of 25 μM $G2_{D187N}$ were investigated using the same inhibitor-to-$G2_{D187N}$ molar ratios (0.1:1, 1:1, and 1:10) employed for the experiments with LB6 (Fig. 5). GAC triggered $G2_{D187N}$ aggregation in a concentration-dependent manner, as evidenced by an earlier onset and a higher fluorescence plateau with ThT fluorescence more pronounced at the highest concentration (Supplementary Table S3). Being the amyloidogenic core of the G2 domain, GAC appears to have a strong propensity to self-aggregate (Supplementary Fig. S7). The two isolated flanking sequences, FS1 and FS2, and the scaffold did not significantly affect the aggregation of $G2_{D187N}$ at both molar ratios. These results are consistent with their structural role within LB6, where they act as an inert barrier that prevents interactions between the aggregating amyloidogenic sequences.

Table 2
Secondary structure content of peptidomimetics computed with Dichroweb from the CD spectra presented in Fig. 4C.

Compound	Helix (%)	β-Sheet (%)	β-Turn (%)	Random (%)
LB6	16	13	17	54
MC35	18	12	16	54
MC45	14	24	17	45

We then tested the effect of MC35, the reverse-sequence peptidomimetic, designed to assess the directionality of the interaction and the importance of conformational flexibility for inhibitory activity. In the ThT fluorescence assays, MC35 displayed a dual concentration-dependent behaviour. At 0.1:1 molar ratio, it slowed $G2_{D187N}$ aggregation, with a lag phase comparable to that observed with LB6 (Supplementary Table S3), while at a 1:1 molar ratio, it triggered $G2_{D187N}$ aggregation (Fig. 5). When tested at the highest concentration, we observed already at time 0, a high fluorescent signal that remained almost constant for up to 18 h (Fig. 5), which could be ascribed to either a strong self-aggregating propensity of MC35 at a higher concentration or an interaction with ThT. These hypotheses were partially confirmed by the fact that MC35 tested alone (Supplementary Fig. S7) exhibited significant ThT fluorescence since time 0, suggesting the presence of preformed aggregates. This behaviour was also confirmed by dynamic light scattering experiments, where MC35 showed a great tendency to aggregate (data not shown). The last tested peptidomimetic, MC45, contains the GAC sequence and the alternative flanking sequence, FS2. This compound, at both the tested concentrations, did not display clear aggregation-inhibitory activity on $G2_{D187N}$ aggregation.

The near absence of antiaggregating activity by the isolated moieties and by MC45, together with the ability of MC35 to exert an inhibitory effect on $G2_{D187N}$ aggregation similar to that of LB6, suggests that the inhibitory activity of LB6 peptidomimetic, is related to the correct orientation of the component and the crucial presence of the correct FS1 flanking sequence.

GSN aggregation occurs in the extracellular space, under oxidative conditions [52,53]. Since $G2_{D187N}$, LB6, and MC35 contain cysteines, analysis in the presence of a reducing agent may help shed light on the mechanism of action of peptidomimetics, such as by excluding the formation of covalent adducts. To this end, the far-UV CD spectra and temperature denaturation ramp, as well as the aggregation kinetics of $G2_{D187N}$, with or without the peptidomimetics, were analysed in the presence of DTT (Supplementary Result 2 and Fig. S8). The reducing agent did not affect the structure of potential inhibitors that do not acquire $G2_{D187N}$ (de)stabilizing properties. In addition, their inhibitory effect on $G2_{D187N}$ aggregation was comparable to that exerted in the absence of DTT, ultimately excluding that the formation of inter- or intra-molecular and intra-species disulfides may contribute to their anti-aggregating activity.

2.5. LB6 and MC35 modify fibril morphology and promote structural remodelling

The possible impact of LB6 and MC35 on the morphology of $G2_{D187N}$ fibrils was investigated. To this end, 100 μM $G2_{D187N}$ was incubated for 15 h in the absence or presence of LB6 or MC35, at 0.1:1 and 1.1 molar ratios, and the samples were analysed by transmission electron microscopy (TEM).

The first anti-aggregating effect observed was a reduction of fibril clusters in low-magnification images (Supplementary Fig. S9A), then confirmed at higher magnifications (Fig. 6A), where fewer and shorter fibrils were present, which also appeared less structurally organized.

Although fibrils are considered less toxic than soluble oligomers, they can accumulate and interact with cell membranes, thereby exacerbating cellular damage. They can also dissociate into smaller, more

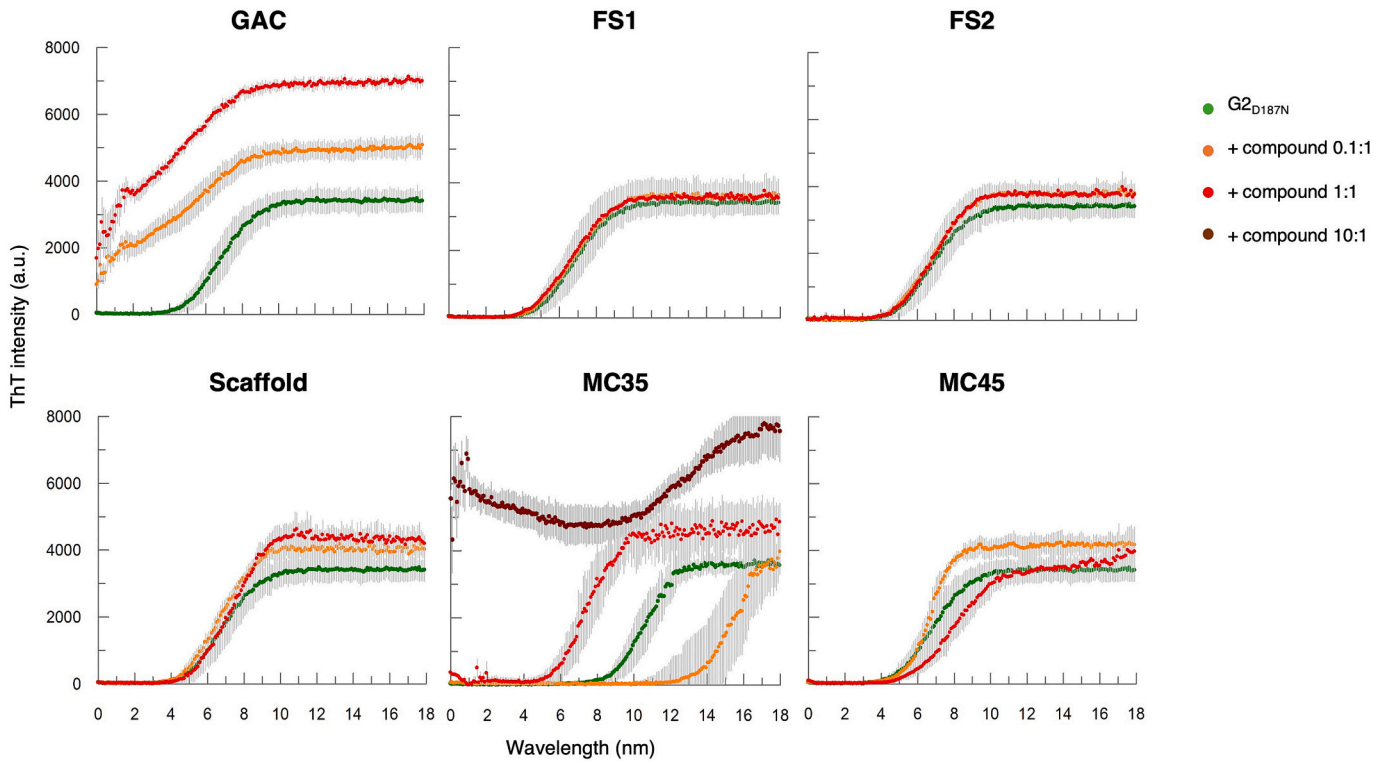

Fig. 5. Effect of single moieties and peptidomimetics on the aggregation of $G2_{D187N}$. ThT fluorescence assays showing the aggregation of 25 μM $G2_{D187N}$ over time in the absence and presence of increasing concentrations of GAC, FS1, FS2, Scaffold, MC35, and MC45. Each data point is the mean ± SD (n = 5).

toxic species [28,29,54,55]. For this reason, an effective antiaggregating compound should not only prevent fibril formation but also prevent existing fibrils from acting as reservoirs of toxic oligomers. To this end, we investigated the ability of LB6 and MC35 to act as disaggregating compounds on mature fibrils, by incubating them for 16 h with $G2_{D187N}$ preformed fibrils at 0.1:1 and 1:1 molar ratios. Although the ThT assays did not reveal any changes in fluorescence upon the compounds' addition (Supplementary Fig. S10), negative-stain TEM images showed a comparable effect for LB6 (at both 0.1:1 and 1:1 molar ratios) and MC35 at the higher concentration tested (1:1 molar ratio), with fewer and less compact fibril clusters (Supplementary Fig. S9B), a reduction in fibril abundance and length, and alterations in fibril morphology (Fig. 6B). The remodelling activity of MC35 at the lowest concentration was, however, less pronounced than that of LB6. These results indicate that LB6 and MC35 interfere with mature fibrils, allowing the formation of smaller aggregated assemblies.

2.6. LB6 and MC35 counteracted the toxicity of $G2_{D187N}$ fibrils in *C. elegans*

Two different *C. elegans*-based experimental approaches were used to investigate whether the ability of the peptidomimetics to inhibit the aggregation of $G2_{D187N}$ and to target its pre-formed fibrils, modifying their morphology, can translate into an *in vivo* protective effect.

To test the ability to protect as anti-aggregating compounds, thus reducing the formation of toxic protein assemblies, LB6 or MC35 were co-incubated with monomeric 100 μM $G2_{D187N}$ at 0.1:1 and 1.1 molar ratios for 16 h. The samples were then diluted 10-fold with 5 mM phosphate-buffered saline (PBS), pH 7.4, to administer 10 μM $G2_{D187N}$ to worms (50 worms/50 μl). PBS was administered alone as a negative control. Twenty-four hours after administration, pharyngeal activity was evaluated as a readout of toxicity. As shown in Fig. 7A, administration of $G2_{D187N}$ alone significantly reduced the pharyngeal function of worms by about 17% compared to controls. This toxicity was similarly reduced when $G2_{D187N}$ was co-incubated with peptidomimetics, with pharyngeal function of ~87% and ~ 92% in worms administered LB6 and MC35 at a 0.1:1 or 1:1 molar ratio, respectively. LB6 and MC35, tested at concentrations corresponding to those used when added at the 0.1:1 and 1:1 molar ratios to 10 μM $G2_{D187N}$, *i.e.*, 1 and 10 μM, did not exert any toxic effect on the pharyngeal function of worms (Supplementary Fig. S11).

We also tested whether the peptidomimetics can interact with pre-formed fibrils, reducing their toxicity. To this end, mature fibrils were obtained by incubating 100 μM monomeric $G2_{D187}$ for 16 h as previously described, and then LB6 and MC35 were added for 16 h at 0.1:1 and 1:1 molar ratios. Samples, diluted tenfold, were then administered to worms, and the pharyngeal function was scored 24 h later. Pre-formed fibrils reduced pharyngeal contraction by ~17%, similarly to what was observed in the previous experimental condition (Fig. 7B). The addition of LB6 and MC35 to pre-formed $G2_{D187N}$ fibrils significantly protected worms from pharyngeal dysfunction by increasing it from 83% to 90% and 94% at 0.1:1 and 1:1 molar ratios, respectively. These findings indicate that the smaller aggregates generated by incubating pre-formed fibrils with peptidomimetics are not toxic for worms.

3. Discussion

AGel is not necessarily a fatal condition; however, it is associated with lifelong morbidity that significantly affects patients' quality of life, that of their caregivers, and a burden for all society [14,15]. The progressive deposition of pathological amyloid fibrils, caused by single-point mutations in the *GSN* gene, leads to a range of debilitating manifestations, including neuropathy, ophthalmologic complications, and cutaneous or systemic involvement, that progressively worsen over time. At present, only symptomatic relief can be achieved through repeated surgical procedures or other invasive therapeutic interventions. Consequently, the development of pharmacological therapies preventing or slowing down amyloid fibril formation, or enhancing clearance of deposited aggregates, is of critical importance. The most common AGel variant is D187Y/N, which ultimately leads to the

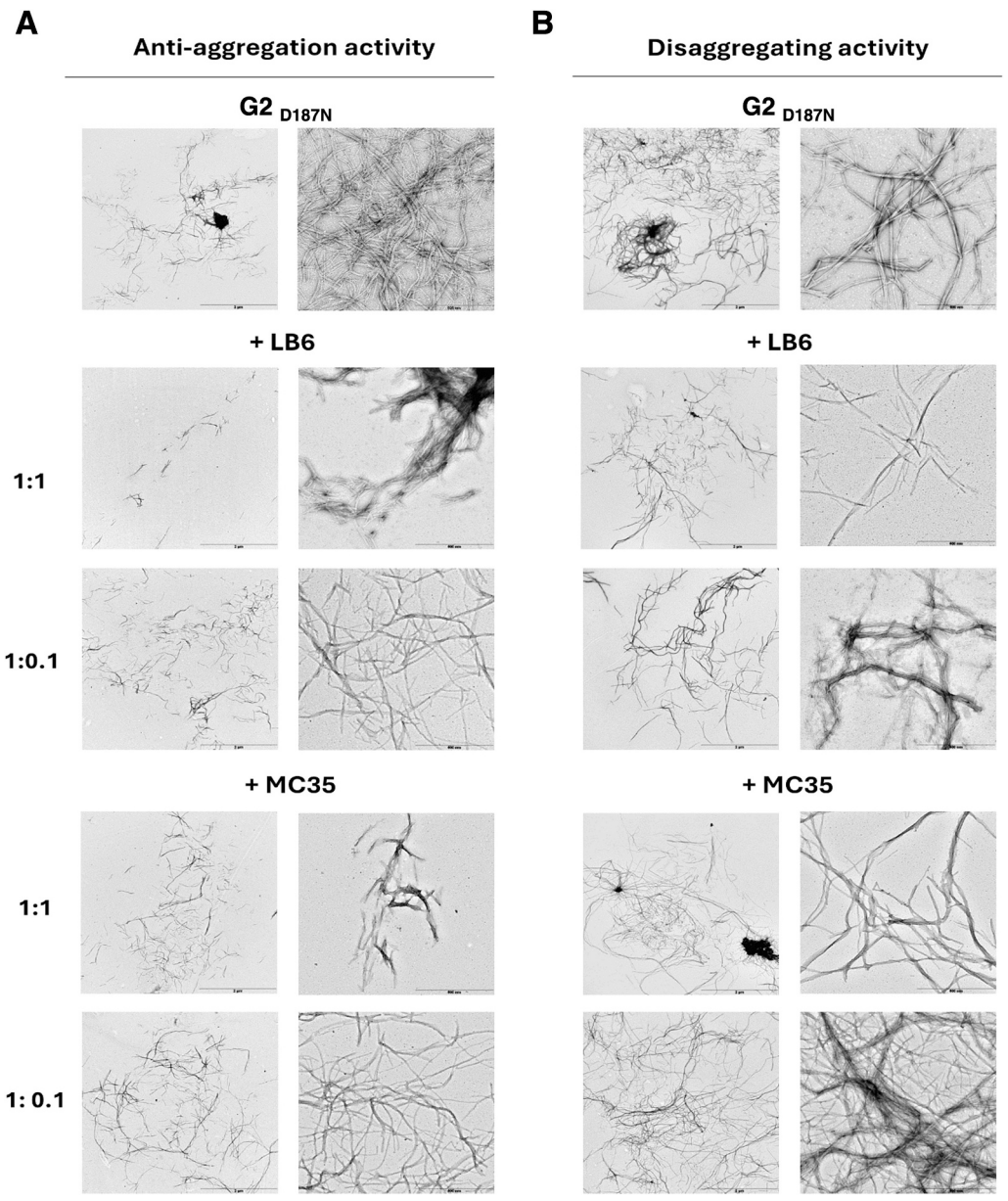

Fig. 6. Morphology remodelling effect of LB6 and MC35 on $G2_{D187N}$ fibers. A) Representative TEM images of monomeric 100 μM $G2_{D187N}$ incubated for 16 h in the absence ($G2_{D187N}$) or presence of LB6 or MC35, at 0.1:1 and 1:1 molar ratios. Scale bars: left column = 2 μm; right column = 500 nm. B) Representative TEM images of $G2_{D187N}$ preformed fibrils incubated for 16 h in the absence or presence of LB6 or MC35 at 0.1:1 and 1:1 molar ratios. Scale bars: left column = 2 μm; right column = 500 nm.

aggregation of two small GSN fragments of 5 and 8 kDa generated through aberrant proteolytic cleavage of the mutant protein, spanning almost the entire G2 domain. Based on the known GSN amylogenic sequence GAC present in the second domain, our group designed three peptidomimetics that interact with the GAC amyloidogenic sequence and interfere with its aggregation [27]. However, GAC aggregation is too fast and does not follow the typical sigmoidal aggregation profile, making it difficult to obtain information on the length of the lag phase, on the rate (slope) of the process, and on the plateau, where the process approaches equilibrium, all of which are crucial to elucidate the mechanism driving G2 aggregation.

In this study, we used $G2_{D187N}$ and showed that primary nucleation likely plays a major role in G2 aggregation, and an ideal inhibitor should target this step to prevent, or at least significantly slow down, the formation of soluble oligomers, considered the most toxic species. In its antiaggregating activity, LB6 slows $G2_{D187N}$ aggregation by inhibiting primary nucleation, and/or other early aggregation events, at sub-stochiometric concentrations, as shown by the elongated lag phase, and almost abolishes aggregation at higher concentrations. The anti-aggregating activity was further validated by excluding any stabilizing effect of the native state. Indeed, we observed no impact of the compounds on the protein's CD spectrum or thermal stability. Same studies, together with ThT assays, in the presence of reducing agents also exclude the formation of covalent adducts between the peptidomimetics and the protein.

LB6 harbours on one arm a portion of the G2 amyloidogenic sequence ($GAC_{182–192}$), on the other, one of the two sequences flanking $GAC_{182–192}$ in the same β-sheet ($FS1_{194–204}$) linked by an unnatural amino acid scaffold. MD simulations, CD, and NMR structural characterization of LB6 showed a disordered structure of the peptidomimetic under physiological conditions. This high conformational flexibility is driven by the conformational freedom of the scaffold's piperidine-

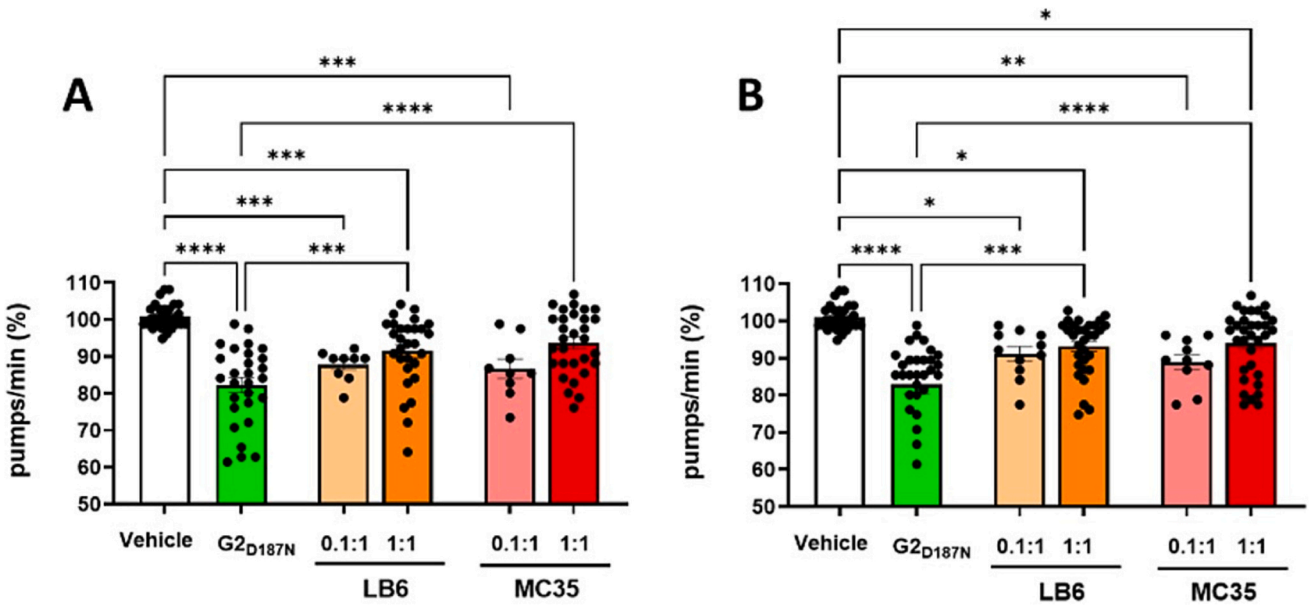

Fig. 7. Toxic effect of $G2_{D187N}$ fibrils in *C. elegans* and the protective effect of the peptidomimetics tested at early and late stages of aggregation. A) Monomeric $G2_{D187N}$ (100 μM) was incubated for 16 h under aggregating conditions in the absence ($G2_{D187N}$) and presence of LB6 and MC35 at 0.1:1 and 1.1 molar ratios. The samples were then diluted 10-fold with 5 mM phosphate-buffered saline (Vehicle), pH 7.4, to administer 10 μM $G2_{D187N}$ to worms (50 worms/50 μl). B) Monomeric $G2_{D187N}$ (100 μM) was incubated for 16 h under aggregating conditions. Fibrils were then incubated for an additional 16 h with LB6 and MC35 at 0.1:1 and 1.1 molar ratios. The samples were then diluted 10-fold with 5 mM phosphate-buffered saline (Vehicle), pH 7.4, to administer 10 μM $G2_{D187N}$ to worms (50 worms/50 μl). In both experiments, vehicle alone was administered as a negative control. Twenty-four hours after the administration, the contraction number of the terminal bulb of the pharynx was scored over a 1-min interval (pumps/min). Data are the mean ± SEM of the percentage of vehicle-treated worms ($N = 30$) from 3 independent experiments. * $p < 0.05$, ** $p < 0.01$, *** $p < 0.001$, and **** $p < 0.0001$ according to one-way ANOVA and Bonferroni *post hoc* test.

pyrrolidine rings. No intramolecular disulfide bridge formation was observed in the timescale monitored for the aggregation process. It can be speculated that LB6 flexibility is crucial for interacting with transient and polymorphic species, such as early oligomers.

Beyond its flexibility, the entire LB6 chemical structure is also crucial for its inhibitory activity; the isolated moieties have no inhibitory activity, and substitution of the flanking sequence with FS2 in MC45 peptide abolished its activity at any tested concentration. MC45 was also characterized by the presence of a β-hairpin conformation, further supporting that conformational flexibility could be an important determinant of biological activity, together with the flanking-sequence amino acid composition. This last assumption was also reinforced by the characterization of MC35, the reversed analogue, which slows down $G2_{D187N}$ aggregation at low concentration, similarly to LB6. However, higher concentration of MC35 seemed to favour either $G2_{D187N}$ aggregation or the self-aggregation of the peptidomimetic. To resolve this ambiguity, aggregation in the presence of LB6 and MC35 was analysed using negative-stain TEM. TEM images showed that LB6, and to a lesser extent MC35, counteract fibrils formation in a concentration-dependent manner and affect the morphology of the aggregates.

More importantly, assays on *C. elegans* showed that both analogues protected from the toxicity associated with $G2_{D187N}$ aggregation. This represents an important finding, as it is consistent with the ability of these compounds to reduce the formation of soluble toxic species supporting the *in vitro* kinetic results. *In vivo* studies also suggested that MC35 is as potent as LB6 in its inhibitory activity, but solubility and self-aggregation issues limit the enthusiasm for the former.

Mature fibrils of GSN, although not primarily responsible for pathogenicity, are a reservoir of toxic species [28,29,54,55]. Thus, we evaluated also the ability of LB6 and MC35 to target pre-formed fibrils by adding them at the plateau phase of $G2_{D187N}$ aggregation. TEM images revealed a concentration-dependent ability to remodel mature fibrils, with LB6 exhibiting greater activity than MC35. We then demonstrated that the effect of LB6 and MC35 on $G2_{D187N}$ fibrils did not result in the formation of toxic species but conferred protection to worms from fibril-induced toxicity.

While $G2_{D187N}$ represents a widely used model system to study gelsolin aggregation, it does not fully recapitulate the fragments found in patients, which derive from proteolytic processing. In addition, aggregation assays were performed under mildly acidic conditions and relatively high protein concentrations to ensure experimental reproducibility. Therefore, further studies will be required to assess the activity of these compounds under more biologically relevant conditions and on disease-relevant fragments. In conclusion, our data showed that LB6 and, to a lesser extent, MC35 effectively inhibit $G2_{D187N}$ aggregation and promote remodelling of pre-formed fibrils without generating toxic species. These findings highlight the potential of LB6 as a promising scaffold for therapeutic development. However, preclinical studies will be necessary to evaluate the protective effect of LB6 in disease-relevant animal models of AGel., In addition, further investigation of these compounds should assess potential drawbacks, such as their instability and pharmacological properties.

4. Materials and methods

4.1. Expression and purification of $G2_{D187N}$

The isolated G2 domain of the GSN protein carrying the D187N substitution ($G2_{D187N}$) was produced as described by Bonì et al. [56]. More details, the sequence and purification protocol can be found in the Supplementary methods. $G2_{D187N}$ was concentrated to 15 mg/ml in a 20 mM Hepes pH 7.4, containing 100 mM NaCl and 1 mM $CaCl_2$, and was stored at −20 °C.

4.2. ThT assays

Aggregation kinetics were monitored using a Thioflavin-T (ThT) fluorescence assay, which exploits the increase of ThT fluorescence upon binding to β-sheet–enriched structures [57]. $G2_{D187N}$ was diluted with 200 mM sodium acetate buffer, pH 5.0, containing 100 mM NaCl, to a

final concentration of 25 μM for the ThT experiments and 100 μM for TEM analyses and *C. elegans* experiments. Aggregation experiments were performed at pH 5.0 to facilitate aggregation kinetics within experimentally accessible timescales, in line with previous studies on gelsolin domains and other amyloidogenic proteins [27]. The solutions were distributed in 96-well low-binding microplates (Corning 3881, Corning Inc. Life Sciences, Acton, MA) (75 μl/well), and the test compounds were added at 0.1:1, 1:1, and 10:1 molar ratios. Then, 20 μM ThT was added, and the samples were incubated at 37 °C under continuous orbital shaking. ThT fluorescence intensity was recorded at excitation wavelength = 448 nm, and emission = 485 nm, every 5 min for 18 h using an Infinite 200 PRO M Plex microplate reader (Tecan). At least three independent experiments, each with five replicates, were performed. Seeds of $G2_{D187N}$ were prepared by aggregation of 25 μM $G2_{D187N}$ under the same conditions. After 16 h, when the ThT value reached the plateau, the aggregation mixture was sonicated at room temperature for 5 min in an Ultrasonic Bath (VWR). Data from representative experiments were averaged and presented with associated SD without any background correction or normalization.

To better quantify the aggregation, the data were fit with the logistic function reported below, which describes general sigmoidal kinetics and has been already used to model amyloid aggregation [58].

$$F(t) = F(0) + A \Big/ \left(1 + e^{\left(-\left(t - t_{half}\right)/\tau\right)}\right)$$

where t is time and $F(t)$ the fluorescence intensity at time t, A the amplitude, t_half the half time of total growth and τ the midpoint of the growth phase, which estimates its steepness. Thus, the length of the lag phase $t\_lag = t\_half - 2\tau$. For the fitting of the data, their processing and normalization we wrote a jupyter notebook that can be found here https://github.com/LoicGirois/ThT-aggregation-assay-analysis, the downloadable file contains all details of the equation and parameters.

4.3. Chemical synthesis of peptides, the scaffold and peptidomimetics

The piperidine-pyrrolidine scaffold was synthesized through a multicomponent cycloaddition reaction (Fig. 8) [50]. The hydrolysed product 1 (0.16 mmol, 0.060 g, 1 eq) was dissolved in CH_2Cl_2 (0.16 mM) and reacted with Ac_2O (1.44 mmol, 0.1 ml, 9 eq). The pH was measured and set at pH = 8 using N,-Diisopropylethylamine (DIEA) (0.48 mmol, 0.174 ml, 3 eq). The reaction was monitored using thin layer chromatography (CH_2Cl_2: MeOH/ 9:1 + 1% AcOH). After 6 h, no progression was noticed so the crude product was purified using flash column chromatography. The scaffold was isolated with a 65% yield. The pure product was characterized by ^1H and ^{13}C NMR (see Supplementary Fig. S18–20).

Microwave-assisted automated SPPS was performed using the well-established Fmoc/tBu protection group strategy [59] on a Rink amide resin with a loading capacity of 0.55 mmol/g with a Liberty Blue synthesizer using a scale of 0.1 mmol. The amino acids concentration was equal to 0.2 M in DMF. DIC and Oxyma were used as coupling reagents (respectively 0.5 and 1 M in DMF) while for the deprotection 20% piperidine in DMF was used. Couplings were performed at 75 °C using 170 W for 15 s and then at 90 °C using 40 W for 110 s. While the deprotection was performed at 75 °C using 155 W for 15 s and then at 90 °C using 50 W for 50 s.

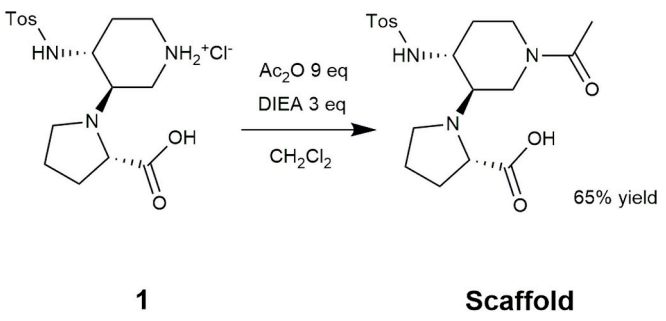

Fig. 8. Structure and synthesis of the Scaffold.

The coupling of the scaffold was performed manually on the resin using HOBt/HBTU/DIEA (1.5/1.5/3 eq) as coupling reagents [27]. The cleavage was then performed using 3 ml of cleavage cocktail for each peptide (trifluoroacetic acid/thioanisole/2,2-(Ethylenedioxy)diethanethiol; 90:7:3) for 3 h at room temperatures. After the cleavage, the peptides were precipitated from ice-cold diethyl ether and recovered by centrifugation at 4 °C. Three diethyl ether washes/centrifugation cycles were carried out to efficiently remove the scavengers. Peptides were purified using an Kinetex C-18 column from Phenomenex (5 μm, 250 × 21.2 mm) by RP-HPLC using different methods but usually using a gradient elution of 20–70% solvent B (solvent A: water/trifluoroacetic acid 100:0.1; solvent B: acetonitrile/trifluoroacetic acid 100:0.1) over 20 min at a flow rate of 20 ml/min. The purified peptides were freeze-dried and stored at −18 °C under N_2. Afterwards, they were analysed using analytical HPLC (20% B for 3 min; 20–70% B over 20 min) and ESI mass spectrometry (Table 3 and Supplementary Fig. S12–17).

4.4. NMR analysis

NMR experiments were performed on a Bruker NEO equipped with a Prodigy cryoprobe operating at 600 MHz. All NMR experiments were acquired at 288 K. LB6 samples for NMR analysis were prepared in phosphate buffer 200 mM pH 5.0, NaCl 100 mM, 5% (*v*/v) D_2O for frequency lock purpose, and LB6 300 μM, as estimated from ^1D ^1H NMR spectrum intensity. Two-dimensional ^1H—^1H TOCSY (mixing 80 ms), ROESY (mixing 250 ms) and NOESY (mixing 100 ms) experiments were performed employing standard Bruker library pulse sequences for LB6 resonances assignment. Matrices of 2048 (t2) by 400 points (t1) were collected. Water suppression was achieved using excitation sculpting with gradients.

For Cα assignment, a 2D 1H—13C HSQC at natural abundance was acquired (matrix of 1024 × 256 points in t2 and t1, respectively).

For NMR data recorded in the presence of a reducing agent, DTT was added in excess relative to the two cysteines. It is worth mentioning that, within the first 24 h, NMR spectra obtained in the presence of DTT are identical to those recorded in the absence of DTT (Supplementary Fig. S1).

TOCSY, ROESY, and NOESY spectra were assigned using Sparky [60]. ^1H-DOSY spectrum was acquired with stimulated echo pulse sequence, and matrix of 2048 (t2) by 80 points (t1) was collected. The z-axis gradient strength varied linearly from 2% to 98% of its maximum value (65.7 G cm − 1), the gradient pulse duration was 4.0 ms, and the time-period between the two gradient pulses was optimized to 50 ms. The relaxation delay D1 was set to 1 s. Water was suppressed using 3–9-19 pulse sequence with gradients. All spectra were manually phased and baseline corrected using TOPSPIN 4.3.0 (Bruker, Karlsruhe, Germany). Self-diffusion coefficients (D) were derived by fitting the NMR data to Stejskal and Tanner equation [61]. The measured D value was fitted with the empirical formula derived from Dudas and coworkers [62] and here reported: logD(IDP) = −0.507logMW – 8.169, giving an estimated molecular weight of 2100 Da, consistent with LB6 MW of 1942 Da.

4.5. Molecular dynamic simulations

Simulation parameters and initial structures for LB6, MC35 and MC45 have been obtained with the LEAP tool in the Amber23 program suite [63]. The forcefield Amber FF14SB [64] has been employed for the natural residues, while the GAFF force field [65] has been used for the synthetic linker. TIP3P water molecules have been added to guarantee a solvation layer of 1.4 nm and chloride anions have been included to neutralize the system's charge. Each solvated peptide has been energy-minimized with the steepest descent algorithm. A 1 ns NVT

Table 3
Structure, purity and quantity of LB6, its analogues and the structural moieties.

	Sequence	MW calculated	MW found	Purity (%)	Mass (mg)
LB6	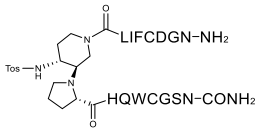	1942,22	1941,829	>99	25
MC35	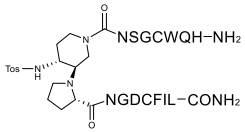	1942,22	1941,82	>99	30
MC45	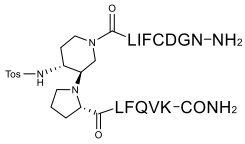	1745,14	1745,89	98	17
GAC	NH_2-LIFCDGN-$CONH_2$	779,91	780,72	98	12
FS1	NH_2-HQWCGSN-$CONH_2$	829,89	831,07	99	30
FS2	NH_2-QRLFQVK-$CONH_2$	917,13	918,01	95	35

equilibration has been performed with the v-rescale thermostat [66] at 300 K, followed by a 1 ns NPT equilibration with the Berendsen barostat. A production simulation for equilibrium AA-MD of 500 ns has been collected in the NPT ensemble with the Parrinello Rahman barostat [67]. A cluster analysis of the production simulation has been performed with gmx cluster tool using the gromos method [68] and a cutoff of 3 Å using Cα as target selection for removal of roto-translation and clustering.

To fully explore the conformational landscape accessible to the peptides, WT-MetaD simulations have been performed starting from the NPT-equilibrated simulation box. The radius of gyration of the peptides and their internal hydrogen bond network have been chosen as collective variables. In particular, the internal H-bond network has been defined based on the hypothetical β-hairpin configuration using the CONTACTMAP CV available in PLUMED and a rational switching function ($r_0 = 0.35$ nm, $d_0 = 0.25$ nm, $n = 6$). Bias potential has been deposited every 1 ps, with initial strength of 2.0 kJ/mol and a biasfactor = 10. For each peptide, five independent WT-metaD simulations of 1 μs each have been collected and the resulting free energy surfaces have been averaged to a single profile.

For the characterization of local ordering of LB6, DSSP (Kabsch & Sander, 1983) analysis was performed with GROMACS. Simulation frames belonging to the two main conformational basins were analysed and the DSSP pattern strings corresponding to D187-I190 and C201-S203 has been isolated. Since the simulated structures have been obtained from different WT-metaD simulations, a reweighting procedure has been applied to account for non-uniform sampling. Each simulated conformation has been projected on the final averaged FES and the corresponding free energy F_i has been used to compute a weight $w_i = e^{-\frac{F_i}{(k_B T)}}$, where k_B is the Boltzmann constant and T the simulation temperature. The probability of a DSSP pattern *ss* has been estimated as $P(ss) = \frac{\sum_{i \subset ss} w_i}{\sum_i w_i}$.

Simulations have been performed with GROMACS-2023.5 [69,70] patched with PLUMED-2.9.0 [71]. Input scripts and configuration files for all systems are publicly available on https://doi.org/10.5281/zenodo.19880178.

4.6. Circular dichroism spectroscopy

The peptides and peptidomimetics conformation was determined by CD experiments (100 μM in HPLC plus water) on a Jasco J-820 spectropolarimeter with a 0.1 cm quartz cuvette. The spectra were recorded from 190 to 250 nm with a 0.2 nm step and 2 s collection time per step, taking four averages and using a sensitivity of 100 mdeg and a scanning speed of 50 nm/min. The spectrum of the solvent was subtracted to eliminate interference from cell, solvent and optical equipment. The CD spectra were plotted as mean residue ellipticity θ (degree * cm^2 * $dmol^{-1}$) *versus* wavelength λ (nm). Noise reduction was obtained using a Fourier transform filter program.

Thermal stability and CD spectra of $G2_{D187N}$ were measured in Jasco J-1100 spectropolarimeter equipped with a peltier unit with a 0.1 cm quartz cuvette. 15 μM $G2_{D187N}$ in 200 mM sodium acetate buffer at pH 5.0 and 100 mM NaCl were evaluated in the presence or absence of LB6 at a molar ratio of 1:1 and with or without 2 mM DTT as previously reported [72]. Briefly, the loss of protein secondary structures was monitored following circular dichroism at 218 nm during a 10 to 99 °C temperature ramp (1 °C/min). Gelsolin G2 thermal denaturation is only partially reversible; therefore, the midpoint of the transition is referred to as an apparent melting temperature and should not be interpreted as a strictly thermodynamic quantity. CD spectra between 250 and 190 nm of the samples were registered before and after the unfolding ramp [73].

4.7. Transmission electron microscopy

Samples were prepared under the same conditions used for the ThT fluorescence assay, employing a final $G2_{D187N}$ concentration of 100 μM. LB6 and MC35 were added at 1:1 and 0.1:1 molar ratios at the start of the aggregation experiments for the anti-aggregation analyses, and after overnight aggregation for disaggregation assessment. 10 l of each sample were deposited on copper grids for 20 min and washed three times with distilled water. After absorbing the excess of the water with Whatman filter paper, the grids were negatively stained with 1.5% uranyl acetate. Images were then obtained with an energy filter transmission electron microscope (EFTEM, ZEISS LIBRA® 120, Carl Zeiss S.p.A., Milano, Italy) coupled with an yttrium aluminium garnet (YAG) scintillator slow-scan CCD camera (Sharp eye, TRS, Milano, Italy).

4.8. C. elegans studies

Bristol N2 UK wild-type worms were obtained from Caenorhabditis Genetics Center (CGC, University of Minnesota, Minneapolis, USA). Worms were grown at 20 °C on solid Nematode Growth Medium (NGM)

seeded with *E. coli* OP50 (CGC). Before the experiments, worms were synchronized by egg-laying and cultured for 72 h at 20 °C on NGM plates spread with OP50 *E. coli* (CGC) as food. Worms were then collected by washing the plates with 1 ml M9 buffer (0.3% potassium dihydrogen phosphate, 0.6% sodium phosphate dibasic, 0.5% sodium chloride, and 1 M magnesium sulphate). Samples were prepared under the same conditions used for the ThT fluorescence assay to investigate the anti-aggregation and disaggregation effects of MC35 and LB6 on the aggregation of the $G2_{D187N}$ domain. Worms were treated with 10 μM of $G2_{D187N}$ alone or together with LB6 and MC35 at the molar ratio 1:1 and 0.1:1. Control worms were treated with LB6 and MC35 alone at the same concentration. Samples were diluted in 10 mM phosphate-buffered saline, pH 7.4, and administered to *C. elegans* (50 worms/50 l) as already described [24]. After 2 h of incubation on orbital shaker, worms were transferred to fresh NGM plates seeded with OP50 *E. coli* and incubated at 20 °C. The pharyngeal activity was determined after 24 h by scoring the number of times the terminal bulb of the pharynx contracted over a 1 min interval (pumps/min).

4.9. Statistical analyses

Synchronized worms obtained by egg-laying were randomly distributed onto NGM plates containing the different treatments to avoid allocation bias. For each experiment, worms were transferred to plates in comparable numbers across groups. All the evaluations were performed blind to the treatment groups. The data were analysed using GraphPad Prism 10.2 software (CA, USA) by one-way ANOVA and Bonferroni's *post hoc* test. A p-value <0.05 was considered significant.

CRediT authorship contribution statement

Michela Bollati: Writing – original draft, Investigation, Data curation, Conceptualization. **Kaliroi Peqini:** Writing – original draft, Investigation, Conceptualization. **Carmina Natale:** Writing – review & editing, Investigation. **Federica Malinverno:** Investigation. **Chiara Leonardi:** Writing – review & editing, Investigation. **Beatrice Bonaldi:** Writing – review & editing, Investigation. **Loic Girois:** Writing – review & editing, Investigation. **Katiuscia Pagano:** Writing – review & editing, Investigation. **Laura Ragona:** Writing – review & editing, Investigation. **Alessandro Corbelli:** Writing – review & editing, Investigation. **Fabio Fiordaliso:** Writing – review & editing, Investigation. **Andrea Grazzi:** Writing – review & editing, Investigation. **Xinyue Gao:** Writing – review & editing, Investigation. **Stefano Pieraccini:** Writing – original draft, Supervision, Conceptualization. **Sara Pellegrino:** Writing – review & editing, Writing – original draft, Supervision, Conceptualization. **Luisa Diomede:** Writing – review & editing, Writing – original draft, Supervision, Conceptualization. **Matteo de Rosa:** Writing – original draft, Supervision, Project administration, Conceptualization.

Declaration of Generative AI and AI-assisted technologies in the writing process

During the preparation of this work, the authors used Copilot (Microsoft) and Grammarly (2024) to assist with improving the language and readability of the text. After using these tools, the authors reviewed and edited the content as needed and take full responsibility for the content of the publication.

Funding

This work was supported by the National Recovery and Resilience Plan (NRRP), Mission 4, Component 2, Investment 1.1, Call for tender No. 104 published on 2.2.2022 by the Italian Ministry of University and Research (MUR), funded by the European Union – NextGenerationEU – Project Title "Novel Approaches to Gelsolin Amyloidosis Treatment – NAGAT" – CUP B53D23015890006;

This work was supported by Fondazione Telethon ETS-Italy (Grant no. GMR24T1097).

K.P. and S.P. thank University of Milan - Piano di sostegno alla Ricerca 2025 - LINEA 2 for funding and the MS facility of the Unitech COSPECT (University of Milan, Italy) for mass spectrometry analyses.

L.R and K.P. acknowledge support from Fondazione Antonio De Marco.

Declaration of competing interest

The authors declare that they have no known competing financial interests or personal relationships that could have appeared to influence the work reported in this paper.

Acknowledgements

We thank Ms. Martina Costa and Claudia Ricci for their technical assistance and Dr. Francesca De Santi (Imati-CNR, Milan, Italy) for helpful discussion.

Appendix A. Supplementary data

Supplementary data to this article can be found online at https://doi.org/10.1016/j.ijbiomac.2026.153423.

Data availability

Data will be made available on request.

References

[1] J. Cabral-Macias, L.A. Garcia-Montaño, M. Pérezpeña-Díazconti, M.-C. Aguilar, G. Garcia, C.I. Vencedor-Meraz, E.O. Graue-Hernandez, O.F. Chacón-Camacho, J. C. Zenteno, Clinical, histopathological, and in silico pathogenicity analyses in a pedigree with familial amyloidosis of the Finnish type (Meretoja syndrome) caused by a novel gelsolin mutation, Mol. Vis. 26 (2020) 345–354.

[2] B. Dansereau, L.H. Wang, M. Ma, Hereditary neuropathic itch caused by gelsolin mutation, J. Neurol. Sci. 463 (2024) 123139, https://doi.org/10.1016/j.jns.2024.123139.

[3] A. De La Chapelle, R. Tolvanen, G. Boysen, J. Santavy, L. Bleeker-Wagemakers, C.P. J. Maury, J. Kere, Gelsolin–derived familial amyloidosis caused by asparagine or tyrosine substitution for aspartic acid at residue 187, Nat. Genet. 2 (1992) 157–160, https://doi.org/10.1038/ng1092-157.

[4] Y.A. Efebera, A. Sturm, E.C. Baack, C.C. Hofmeister, A. Satoskar, T. Nadasdy, G. Nadasdy, D.M. Benson, J.D. Gillmore, P.N. Hawkins, D. Rowczenio, Novel gelsolin variant as the cause of nephrotic syndrome and renal amyloidosis in a large kindred, Amyloid 21 (2014) 110–112, https://doi.org/10.3109/13506129.2014.891502.

[5] S. Gavinda, B. Anthony, D. Michael, E. Cerys, H. Alison, T. Kevin, 276 A new face for an old foe? J. Neurol. Neurosurg. Psychiatry 89 (2018) https://doi.org/10.1136/jnnp-2018-ABN.140. A40.3-A40.

[6] H. Liang, H. Zheng, J. Lin, K. Lin, A novel heterozygous mutation in the gelsolin gene causes Finnish gelsolin amyloidosis associated with nephropathy and thrombotic microangiopathy, Arch. Med. Sci. (2025), https://doi.org/10.5114/aoms/202433.

[7] L. Mendelson, T. Prokaeva, K.H.V. Lau, V. Sanchorawala, K. McCausland, B. Spencer, S. Dasari, E.D. McPhail, M.C. Kaku, Hereditary gelsolin amyloidosis: a rare cause of cranial, peripheral and autonomic neuropathies linked to D187N and Y447H substitutions, Amyloid 30 (2023) 357–363, https://doi.org/10.1080/13506129.2023.2204999.

[8] J. Meretoja, Familial systemic paramyloidosis with lattice dystrophy of the cornea, progressive cranial neuropathy, skin changes and various internal symptoms. A previously unrecognized heritable syndrome, Ann. Clin. Res. 1 (1969) 314–324.

[9] S. Mullany, E. Souzeau, S. Klebe, T. Zhou, L.S.W. Knight, A. Qassim, E.C. Berry, H. Marshall, M. Hussey, A. Dubowsky, J. Breen, M.M. Hassall, R.A. Mills, J. E. Craig, O.M. Siggs, A novel GSN variant outside the G2 calcium-binding domain associated with amyloidosis of the Finnish type, Hum. Mutat. 42 (2021) 818–826, https://doi.org/10.1002/humu.24214.

[10] K.Z. Oregel, G.P. Shouse, C. Oster, F. Martinez, J. Wang, M. Rosenzweig, J. K. Deisch, C.-S. Chen, G. Nagaraj, Atypical Presentation of Gelsolin Amyloidosis in a Man of African Descent with a Novel Mutation in the Gelsolin Gene, Am. J. Case Rep. 19 (2018) 374–381, https://doi.org/10.12659/AJCR.907550.

[11] M. Potrč, M. Volk, M. De Rosa, J. Pižem, N. Teran, H. Jaklič, A. Maver, B. Drnovšek-Olup, M. Bollati, K. Vogelnik, A. Hočevar, A. Gornik, V. Pfeifer, B. Peterlin, M. Hawlina, A. Fakin, Clinical and histopathological features of gelsolin amyloidosis associated with a novel GSN variant p.Glu580Lys, Int. J. Mol. Sci. 22 (2021) 1084, https://doi.org/10.3390/ijms22031084.

[12] A. Roldán-Sevilla, M. Gallego-Delgado, M.T. Lista-Araujo, J. Torres-Pérez, A. M. Merino-Merino, C. Gil-Polo, D. Cantero-Lozano, S.M. Lorenzo-Hernandez, R. Eiros-Bachiller, Clinical and genetic features of AGel amyloidosis caused by novel gelsolin variant and its impact on cardiac function and conduction disorders, Amyloid 32 (2025) 90–92, https://doi.org/10.1080/13506129.2024.2441784.

[13] S. Sethi, J.D. Theis, P. Quint, W. Maierhofer, P.J. Kurtin, A. Dogan, E. W. Highsmith, Renal amyloidosis associated with a novel sequence variant of gelsolin, Am. J. Kidney Dis. 61 (2013) 161–166, https://doi.org/10.1053/j.ajkd.2012.07.016.

[14] T. Nikoskinen, E.-K. Schmidt, D. Strbian, S. Kiuru-Enari, S. Atula, Natural course of Finnish gelsolin amyloidosis, Ann. Med. 47 (2015) 506–511, https://doi.org/10.3109/07853890.2015.1075063.

[15] E.-K. Schmidt, S. Atula, M. Tanskanen, T. Nikoskinen, I.-L. Notkola, S. Kiuru-Enari, Causes of death and life span in Finnish gelsolin amyloidosis, Ann. Med. 48 (2016) 352–358, https://doi.org/10.1080/07853890.2016.1177197.

[16] J. Feldt, M. Schicht, F. Garreis, J. Welss, U.W. Schneider, F. Paulsen, Structure, regulation and related diseases of the actin-binding protein gelsolin, Expert Rev. Mol. Med. 20 (2018) e7, https://doi.org/10.1017/erm.2018.7.

[17] D.J. Kwiatkowski, T.P. Stossel, S.H. Orkin, J.E. Mole, H.R. Coltens, H.L. Yin, Plasma and cytoplasmic gelsolins are encoded by a single gene and contain a duplicated actin-binding domain, Nature 323 (1986) 455–458, https://doi.org/10.1038/323455a0.

[18] S. Nag, M. Larsson, R.C. Robinson, L.D. Burtnick, Gelsolin: The tail of a molecular gymnast, Cytoskeleton 70 (2013) 360–384, https://doi.org/10.1002/cm.21117.

[19] S. Nag, Q. Ma, H. Wang, S. Chumnarnsilpa, W.L. Lee, M. Larsson, B. Kannan, M. Hernandez-Valladares, L.D. Burtnick, R.C. Robinson, Ca^{2+} binding by domain 2 plays a critical role in the activation and stabilization of gelsolin, Proc. Natl. Acad. Sci. 106 (2009) 13713–13718, https://doi.org/10.1073/pnas.0812374106.

[20] H.Q. Sun, M. Yamamoto, M. Mejillano, H.L. Yin, Gelsolin, a Multifunctional Actin Regulatory Protein, J. Biol. Chem. 274 (1999) 33179–33182, https://doi.org/10.1074/jbc.274.47.33179.

[21] H. Zorgati, M. Larsson, W. Ren, A.Y.L. Sim, J. Gettemans, J.M. Grimes, W. Li, R. C. Robinson, The role of gelsolin domain 3 in familial amyloidosis (Finnish type), Proc. Natl. Acad. Sci. 116 (2019) 13958–13963, https://doi.org/10.1073/pnas.1902189116.

[22] M. Sridharan, W.E. Highsmith, P.J. Kurtin, M.T. Zimmermann, J.D. Theis, S. Dasari, D. Dingli, A Patient With Hereditary ATTR and a Novel AGel p. Ala578Pro Amyloidosis, Mayo Clin. Proc. 93 (2018) 1678–1682, https://doi.org/10.1016/j.mayocp.2018.06.016.

[23] C.-D. Chen, Furin initiates gelsolin familial amyloidosis in the Golgi through a defect in Ca2+ stabilization, EMBO J. 20 (2001) 6277–6287, https://doi.org/10.1093/emboj/20.22.6277.

[24] T. Giorgino, D. Mattioni, A. Hassan, M. Milani, E. Mastrangelo, A. Barbiroli, A. Verhelle, J. Gettemans, M.M. Barzago, L. Diomede, M. de Rosa, Nanobody interaction unveils structure, dynamics and proteotoxicity of the Finnish-type amyloidogenic gelsolin variant, Biochim. Biophys. Acta Mol. basis Dis. 1865 (2019) 648–660, https://doi.org/10.1016/j.bbadis.2019.01.010.

[25] C.P. Maury, E.L. Nurmiaho-Lassila, H. Rossi, Amyloid fibril formation in gelsolin-derived amyloidosis. Definition of the amyloidogenic region and evidence of accelerated amyloid formation of mutant Asn-187 and Tyr-187 gelsolin peptides, Lab. Investig. J. Tech. Methods Pathol. 70 (1994) 558–564.

[26] J.P. Solomon, I.T. Yonemoto, A.N. Murray, J.L. Price, E.T. Powers, W.E. Balch, J. W. Kelly, The 8 and 5 kDa Fragments of plasma gelsolin form amyloid fibrils by a nucleated polymerization mechanism, while the 68 kDa fragment is not amyloidogenic, Biochemistry 48 (2009) 11370–11380, https://doi.org/10.1021/bi901368e.

[27] M. Bollati, K. Peqini, L. Barone, C. Natale, M. Beeg, M. Gobbi, L. Diomede, M. Trucchi, M. De Rosa, S. Pellegrino, Rational design of a peptidomimetic inhibitor of gelsolin amyloid aggregation, Int. J. Mol. Sci. 23 (2022) 13973, https://doi.org/10.3390/ijms232213973.

[28] F. Chiti, C.M. Dobson, Protein Misfolding, Amyloid Formation, and Human Disease: A Summary of Progress Over the Last Decade, Annu. Rev. Biochem. 86 (2017) 27–68, https://doi.org/10.1146/annurev-biochem-061516-045115.

[29] T.P.J. Knowles, M. Vendruscolo, C.M. Dobson, The amyloid state and its association with protein misfolding diseases, Nat. Rev. Mol. Cell Biol. 15 (2014) 384–396, https://doi.org/10.1038/nrm3810.

[30] H.J. Lachmann, H.J.B. Goodman, J.A. Gilbertson, J.R. Gallimore, C.A. Sabin, J. D. Gillmore, P.N. Hawkins, Natural history and outcome in systemic AA amyloidosis, N. Engl. J. Med. 356 (2007) 2361–2371, https://doi.org/10.1056/NEJMoa070265.

[31] G. Merlini, D.C. Seldin, M.A. Gertz, Amyloidosis: pathogenesis and new therapeutic options, J. Clin. Oncol. Off. J. Am. Soc. Clin. Oncol. 29 (2011) 1924–1933, https://doi.org/10.1200/JCO.2010.32.2271.

[32] L. Leimu, P. Holm, A. Gąciarz, O. Haavisto, S. Prince, U. Pesonen, T. Huovinen, U. Lamminmäki, Epitope-specific antibody fragments block aggregation of AGelD187N, an aberrant peptide in gelsolin amyloidosis, J. Biol. Chem. 300 (2024) 107507, https://doi.org/10.1016/j.jbc.2024.107507.

[33] A. Van Den Abbeele, S. De Clercq, A. De Ganck, V. De Corte, B. Van Loo, S.H. Soror, V. Srinivasan, J. Steyaert, J. Vandekerckhove, J. Gettemans, A llama-derived gelsolin single-domain antibody blocks gelsolin–G-actin interaction, Cell. Mol. Life Sci. 67 (2010) 1519–1535, https://doi.org/10.1007/s00018-010-0266-1.

[34] W. Van Overbeke, J. Wongsantichon, I. Everaert, A. Verhelle, O. Zwaenepoel, A. Loonchanta, L.D. Burtnick, A. De Ganck, T. Hochepied, J. Haigh, C. Cuvelier, W. Derave, R.C. Robinson, J. Gettemans, An ER-directed gelsolin nanobody targets the first step in amyloid formation in a gelsolin amyloidosis mouse model, Hum. Mol. Genet. 24 (2015) 2492–2507, https://doi.org/10.1093/hmg/ddv010.

[35] W. Van Overbeke, A. Verhelle, I. Everaert, O. Zwaenepoel, J. Vandekerckhove, C. Cuvelier, W. Derave, J. Gettemans, Chaperone Nanobodies Protect Gelsolin Against MT1-MMP Degradation and Alleviate Amyloid Burden in the Gelsolin Amyloidosis Mouse Model, Mol. Ther. 22 (2014) 1768–1778, https://doi.org/10.1038/mt.2014.132.

[36] A. Verhelle, N. Nair, I. Everaert, W. Van Overbeke, L. Supply, O. Zwaenepoel, C. Peleman, J. Van Dorpe, T. Lahoutte, N. Devoogdt, W. Derave, M.K. Chuah, T. VandenDriessche, J. Gettemans, AAV9 delivered bispecific nanobody attenuates amyloid burden in the gelsolin amyloidosis mouse model, Hum. Mol. Genet. 26 (2017) 1353–1364, https://doi.org/10.1093/hmg/ddx056.

[37] A. Verhelle, W. Van Overbeke, C. Peleman, R. De Smet, O. Zwaenepoel, T. Lahoutte, J. Van Dorpe, N. Devoogdt, J. Gettemans, Non-Invasive Imaging of Amyloid Deposits in a Mouse Model of AGel Using 99mTc-Modified Nanobodies and SPECT/CT, Mol. Imaging Biol. 18 (2016) 887–897, https://doi.org/10.1007/s11307-016-0960-y.

[38] M. Ahmad, J. Esposto, C. Golec, C. Wu, S. Martic-Milne, Aggregation of gelsolin wild-type and G167K/R, N184K, and D187N/Y mutant peptides and inhibition, Mol. Cell. Biochem. 476 (2021) 2393–2408, https://doi.org/10.1007/s11010-021-04085-6.

[39] P. Arya, A. Srivastava, S.V. Vasaikar, G. Mukherjee, P. Mishra, B. Kundu, Selective interception of gelsolin amyloidogenic stretch results in conformationally distinct aggregates with reduced toxicity, ACS Chem. Neurosci. 5 (2014) 982–992, https://doi.org/10.1021/cn500002v.

[40] A.K. Mahalka, C.P.J. Maury, P.K.J. Kinnunen, 1-Palmitoyl-2-(9′-oxononanoyl)- *sn* -glycero-3-phosphocholine, an Oxidized Phospholipid, Accelerates Finnish Type Familial Gelsolin Amyloidosis in Vitro, Biochemistry 50 (2011) 4877–4889, https://doi.org/10.1021/bi200195s.

[41] D. Di Lorenzo, N. Bisi, J. Kaffy, L.M. Ramirez, M. Zweckstetter, O. Lequin, I. Garfagnini, J. Luo, Y. Hannappel, I. Ennen, V. Dodero, N. Sewald, M.L. Gelmi, N. Tonali, R. Brandt, S. Ongeri, Synthetic chaperone based on Hsp90-Tau interaction inhibits Tau aggregation and rescues physiological Tau-Microtubule interaction, Nat. Commun. 16 (2025) 8756, https://doi.org/10.1038/s41467-025-63824-1.

[42] N. Bisi, J. Kothuis, J. Kaffy, H. Pérez Peña, C. Schulz, C.M.G. De Luca, A. Ciullini, I. L. Dellarole, L. Radal, F. Moda, G. Cappelletti, D. Horvath, S. Pieraccini, W. Hoyer, F. Halgand, N. Tonali, S. Ongeri, Peptidomimetics Inspired by α-Synuclein or Its Chaperone αB-Crystallin Differentially Modulate α-Synuclein Aggregation, J. Med. Chem. 69 (2026) 4059–4077, https://doi.org/10.1021/acs.jmedchem.5c02716.

[43] J. Lesma, F. Bizet, C. Berardet, N. Tonali, S. Pellegrino, M. Taverna, L. Khemtemourian, J.-L. Soulier, C. Van Heijenoort, F. Halgand, T. Ha-Duong, J. Kaffy, S. Ongeri, β-Hairpin peptide mimics decrease human islet amyloid polypeptide (hIAPP) aggregation, Front. Cell Dev. Biol. 9 (2021) 729001, https://doi.org/10.3389/fcell.2021.729001.

[44] A. Barducci, G. Bussi, M. Parrinello, Well-Tempered Metadynamics: A Smoothly Converging and Tunable Free-Energy Method, Phys. Rev. Lett. 100 (2008) 020603, https://doi.org/10.1103/PhysRevLett.100.020603.

[45] G. Bussi, F.L. Gervasio, A. Laio, M. Parrinello, Free-Energy Landscape for β Hairpin Folding from Combined Parallel Tempering and Metadynamics, J. Am. Chem. Soc. 128 (2006) 13435–13441, https://doi.org/10.1021/ja062463w.

[46] G. Saladino, S. Pieraccini, S. Rendine, T. Recca, P. Francescato, G. Speranza, M. Sironi, Metadynamics Study of a β-Hairpin Stability in Mixed Solvents, J. Am. Chem. Soc. 133 (2011) 2897–2903, https://doi.org/10.1021/ja105030m.

[47] W. Kabsch, C. Sander, Dictionary of protein secondary structure: Pattern recognition of hydrogen-bonded and geometrical features, Biopolymers 22 (1983) 2577–2637, https://doi.org/10.1002/bip.360221211.

[48] S.L. Kazmirski, R.L. Isaacson, C. An, A. Buckle, C.M. Johnson, V. Daggett, A. R. Fersht, Loss of a metal-binding site in gelsolin leads to familial amyloidosis–Finnish type, Nat. Struct. Biol. 9 (2002) 112–116, https://doi.org/10.1038/nsb745.

[49] M. Törnquist, T.C.T. Michaels, K. Sanagavarapu, X. Yang, G. Meisl, S.I.A. Cohen, T. P.J. Knowles, S. Linse, Secondary nucleation in amyloid formation, Chem. Commun. 54 (2018) 8667–8684, https://doi.org/10.1039/C8CC02204F.

[50] S. Pellegrino, A. Contini, M.L. Gelmi, L. Lo Presti, R. Soave, E. Erba, Asymmetric Modular Synthesis of a Semirigid Dipeptide Mimetic by Cascade Cycloaddition/Ring Rearrangement and Borohydride Reduction, J. Org. Chem. 79 (2014) 3094–3102, https://doi.org/10.1021/jo500237j.

[51] A. Abdul-Gader, A.J. Miles, B.A. Wallace, A reference dataset for the analyses of membrane protein secondary structures and transmembrane residuesusing circular dichroism spectroscopy, Bioinformatics 27 (2011) 1630–1636, https://doi.org/10.1093/bioinformatics/btr234.

[52] S. Kiuru, Gelsolin-related familial amyloidosis, Finnish type (FAF), and its variants found worldwide, Amyloid 5 (1998) 55–66, https://doi.org/10.3109/13506129809007291.

[53] T. Paunlo, H. Kangas, N. Kalkklnen, M. Haltia, J. Palo, L. Peltonen, Toward understanding the pathogenic mechanisms in gelsolin-related amyloidosis: *in vitro* expression reveals an abnormal gelsolin fragment, Hum. Mol. Genet. 3 (1994) 2223–2229, https://doi.org/10.1093/hmg/3.12.2223.

[54] S. Gandy, A.J. Simon, J.W. Steele, A.L. Lublin, J.J. Lah, L.C. Walker, A.I. Levey, G. A. Krafft, E. Levy, F. Checler, C. Glabe, W.B. Bilker, T. Abel, J. Schmeidler, M. E. Ehrlich, Days to criterion as an indicator of toxicity associated with human Alzheimer amyloid-beta oligomers, Ann. Neurol. 68 (2010) 220–230, https://doi.org/10.1002/ana.22052.

[55] U. Sengupta, A.N. Nilson, R. Kayed, The role of amyloid-β oligomers in toxicity, propagation, and immunotherapy, EBioMedicine 6 (2016) 42–49, https://doi.org/10.1016/j.ebiom.2016.03.035.

[56] F. Bonì, M. Milani, R. Porcari, A. Barbiroli, S. Ricagno, M. De Rosa, Molecular basis of a novel renal amyloidosis due to N184K gelsolin variant, Sci. Rep. 6 (2016) 33463, https://doi.org/10.1038/srep33463.
[57] H. LeVine, Thioflavine T interaction with synthetic Alzheimer's disease beta-amyloid peptides: detection of amyloid aggregation in solution, Protein Sci. 2 (1993) 404–410, https://doi.org/10.1002/pro.5560020312.
[58] L. Nielsen, R. Khurana, A. Coats, S. Frokjaer, J. Brange, S. Vyas, V.N. Uversky, A. L. Fink, Effect of Environmental Factors on the Kinetics of Insulin Fibril Formation: Elucidation of the Molecular Mechanism, Biochemistry 40 (2001) 6036–6046, https://doi.org/10.1021/bi002555c.
[59] K. Peqini, S. Attanasio, L. Feni, G. Cappelletti, S. Pellegrino, Breaking down and building up alpha-synuclein: an insight on its N-terminal domain, J. Pept. Sci. 30 (2024) e3556, https://doi.org/10.1002/psc.3556.
[60] W. Lee, M. Tonelli, J.L. Markley, NMRFAM-SPARKY: enhanced software for biomolecular NMR spectroscopy, Bioinformatics 31 (2015) 1325–1327, https://doi.org/10.1093/bioinformatics/btu830.
[61] E.O. Stejskal, J.E. Tanner, Spin Diffusion Measurements: Spin Echoes in the Presence of a Time-Dependent Field Gradient, J. Chem. Phys. 42 (1965) 288–292, https://doi.org/10.1063/1.1695690.
[62] E.F. Dudás, A. Bodor, Quantitative, Diffusion NMR Based Analytical Tool To Distinguish Folded, Disordered, and Denatured Biomolecules, Anal. Chem. 91 (2019) 4929–4933, https://doi.org/10.1021/acs.analchem.8b05617.
[63] D.A. Case, T.E. Cheatham, T. Darden, H. Gohlke, R. Luo, K.M. Merz, A. Onufriev, C. Simmerling, B. Wang, R.J. Woods, The Amber biomolecular simulation programs, J. Comput. Chem. 26 (2005) 1668–1688, https://doi.org/10.1002/jcc.20290.
[64] J.A. Maier, C. Martinez, K. Kasavajhala, L. Wickstrom, K.E. Hauser, C. Simmerling, ff14SB: Improving the Accuracy of Protein Side Chain and Backbone Parameters from ff99SB, J. Chem. Theory Comput. 11 (2015) 3696–3713, https://doi.org/10.1021/acs.jctc.5b00255.
[65] K.G. Sprenger, V.W. Jaeger, J. Pfaendtner, The General AMBER Force Field (GAFF) Can Accurately Predict Thermodynamic and Transport Properties of Many Ionic Liquids, J. Phys. Chem. B 119 (2015) 5882–5895, https://doi.org/10.1021/acs.jpcb.5b00689.
[66] G. Bussi, D. Donadio, M. Parrinello, Canonical sampling through velocity rescaling, J. Chem. Phys. 126 (2007) 014101, https://doi.org/10.1063/1.2408420.
[67] M. Parrinello, A. Rahman, Polymorphic transitions in single crystals: A new molecular dynamics method, J. Appl. Phys. 52 (1981) 7182–7190, https://doi.org/10.1063/1.328693.
[68] X. Daura, K. Gademann, B. Jaun, D. Seebach, W.F. Van Gunsteren, A.E. Mark, Peptide folding: when simulation meets experiment, Angew. Chem. Int. Ed. 38 (1999) 236–240, https://doi.org/10.1002/(SICI)1521-3773(19990115)38:1/2%3C236::AID-ANIE236%3E3.0.CO;2-M.
[69] M.J. Abraham, T. Murtola, R. Schulz, S. Páll, J.C. Smith, B. Hess, E. Lindahl, GROMACS: high performance molecular simulations through multi-level parallelism from laptops to supercomputers, SoftwareX 1–2 (2015) 19–25, https://doi.org/10.1016/j.softx.2015.06.001.
[70] H.J.C. Berendsen, D. Van Der Spoel, R. Van Drunen, GROMACS: A message-passing parallel molecular dynamics implementation, Comput. Phys. Commun. 91 (1995) 43–56, https://doi.org/10.1016/0010-4655(95)00042-E.
[71] G.A. Tribello, M. Bonomi, D. Branduardi, C. Camilloni, G. Bussi, PLUMED 2: New feathers for an old bird, Comput. Phys. Commun. 185 (2014) 604–613, https://doi.org/10.1016/j.cpc.2013.09.018.
[72] M. De Rosa, A. Barbiroli, F. Bonì, E. Scalone, D. Mattioni, M.A. Vanoni, M. Patrone, M. Bollati, E. Mastrangelo, T. Giorgino, M. Milani, The structure of N184K amyloidogenic variant of gelsolin highlights the role of the H-bond network for protein stability and aggregation properties, Eur. Biophys. J. 49 (2020) 11–19, https://doi.org/10.1007/s00249-019-01409-9.
[73] F. Bonì, M. Milani, A. Barbiroli, L. Diomede, E. Mastrangelo, M. De Rosa, Gelsolin pathogenic Gly167Arg mutation promotes domain-swap dimerization of the protein, Hum. Mol. Genet. 27 (2018) 53–65, https://doi.org/10.1093/hmg/ddx383.
[74] M. Bollati, E. Scalone, F. Bonì, E. Mastrangelo, T. Giorgino, M. Milani, M. De Rosa, High-resolution crystal structure of gelsolin domain 2 in complex with the physiological calcium ion, Biochem. Biophys. Res. Commun. 518 (2019) 94–99, https://doi.org/10.1016/j.bbrc.2019.08.013.